Acta Mech 224, 307–326 (2013)
DOI 10.1007/s00707-012-0750-9

Giorgio Riccardi

An analytical study of the self-induced inviscid dynamics of two-dimensional uniform vortices

Received: 16 May 2012 / Published online: 9 November 2012

Abstract The self-induced dynamics of a uniform planar vortex in an isochoric, inviscid fluid is analytically investigated, by writing a new nonlinear integrodifferential problem which describes the time evolution of the Schwarz function of its boundary. In order to overcome the difficulties related to the nonlinear nature of the problem, an approximate solution of the above problem is proposed in terms of a hierarchy of linear integral equations. In particular, the solution at the first order is here investigated and applied to a class of uniform vortices, the kinematics of which is well known. A rich mathematical phenomenology has been found behind the approximate dynamics. In particular, the motion of certain branch points and the consequent changes in the algebraic structure of the Schwarz function appear to be its key features. The approximate solutions are finally compared with the contour dynamics simulations of the vortex motion. The agreement is satisfactory up to times of the order of a quarter of the eddy turnover time, while it becomes more and more qualitative at later times. Eventually, the physical meaning of the approximate solutions is lost, the corresponding vortex boundaries becoming non-simple curves.

1 Introduction

The two-dimensional dynamics of uniform vortices in an isochoric, inviscid fluid is a quite old issue (see e.g. [1] for a recent worldwide view), so that nowadays the main mathematical features of such flows have been well understood. Existence of a unique solution and conservation of its regularity properties have been proved for all times [2–4], encouraged by numerical experiments [5,6]. One could conclude, at least from the point of view of a pure Mathematician, that the problem has been solved.

Unfortunately, applications require much more than existence, uniqueness and regularity of the solutions, so that the understanding of the dynamics of a uniform vortex (e.g. what is the mechanism responsible for the formation of a filament?) still remains a formidable task. This is essentially due to the strongly nonlinear nature of the integrodifferential problem that describes the vortex motion and to the lack of a simple relation between vortex shape and velocity. The second difficulty has recently been overcome, specifying the relation between kinematics and shape of the vortex in a more general context with respect to the one in the literature [7].

The time evolution of a uniform vortex P is on the whole defined by the motion of its boundary ∂P, which is usually investigated by following the so-called *contour dynamics approach*. This method is based on an one-dimensional form of the self-induced velocity $\boldsymbol{u}$, which is reduced to a line integral on ∂P thanks to the uniformity of the vorticity ω inside the vortex. In more detail, consider a material particle which starts from a

G. Riccardi (✉)
Department of Aerospace and Mechanical Engineering,
Second University of Naples, via Roma, 29, 81031 Aversa, CE, Italy
E-mail: giorgio.riccardi@unina2.it

point $\boldsymbol{\xi}$ on the initial ($t = 0$) boundary. At any successive time t (>0), its position $\boldsymbol{x}(\boldsymbol{\xi}; t)$ solves the strongly nonlinear integrodifferential problem:

$$\begin{cases} \partial_t \boldsymbol{x}(\boldsymbol{\xi}; t) = \boldsymbol{u}[\boldsymbol{x}(\boldsymbol{\xi}; t); t] = -\dfrac{\omega}{2\pi} \displaystyle\int_{\partial P(t)} \mathrm{d}\boldsymbol{y} \log |\boldsymbol{x}(\boldsymbol{\xi}; t) - \boldsymbol{y}| \\ \boldsymbol{x}(\boldsymbol{\xi}; 0) = \boldsymbol{\xi}. \end{cases} \tag{1}$$

In the numerical simulations of the motion [8,9], the solution of the problem (1) is approximated by considering only a finite set of points on ∂P, the velocities of which are given by suitable approximations of $\boldsymbol{u}$. Interpolation formulae are used to rebuild an approximation of ∂P, when it is needed. Finally, first integrals of the motion (as the circulation and the second-order moment) are usually employed to check the overall accuracy of the integration.

Despite its apparent simplicity, the velocity $\boldsymbol{u}$ in the problem (1) leads to formidable analytical difficulties even in the study of the kinematics, the shape of the vortex playing a rather involved role. Progresses have been recently achieved by means of the use of the Schwarz function[1] of the curve ∂P. As is well known, the Schwarz function $\boldsymbol{\Phi}$ of the smooth curve ∂P in the plane of the complex variable $x_1 + \boldsymbol{i}\, x_2 = \boldsymbol{x}$ satisfies the request: $\boldsymbol{\Phi} = x_1 - \boldsymbol{i}\, x_2 = \overline{\boldsymbol{x}}$ in any point $\boldsymbol{x}$ belonging to that curve. Generally speaking, $\boldsymbol{\Phi}$ can be analytically continued on a suitable neighbourhood of ∂P. Its singularities can lie inside as well as outside the vortex. Once the Schwarz function of the vortex boundary is known, the conjugate velocity $\overline{\boldsymbol{u}}$ (i.e. the conjugate of the velocity viewed as a complex number, instead of a two-dimensional vector) induced by the vortex in any point $\boldsymbol{x}$ of the plane is written [11] as:

$$\overline{\boldsymbol{u}}(\boldsymbol{x}, \overline{\boldsymbol{x}}; t) = \frac{\omega}{2\boldsymbol{i}} \left[\chi_{P(t)}(\boldsymbol{x})\, \overline{\boldsymbol{x}} + \frac{1}{2\pi \boldsymbol{i}} \int_{\partial P(t)} \mathrm{d}\boldsymbol{y} \frac{\boldsymbol{\Phi}(\boldsymbol{y}; t)}{\boldsymbol{x} - \boldsymbol{y}} \right], \tag{2}$$

χ_P being the characteristic function of P (it holds 1 inside P, 0 outside P and just 1/2 on the boundary) and the integral being evaluated in its principal value if $\boldsymbol{x} \in \partial P$. The new form (2) opens the way to understand the kinematic role of the vortex shape, which is clearly involved in terms of the Schwarz function of the boundary. Moreover, the analytical evaluation of the conjugate velocity (2) can be often performed by means of standard tools of the complex analysis.

Irrespective of the form of the velocity that is used, the problem (1) fails to be useful from an analytical point of view. As a matter of fact it is strongly nonlinear, so that its analytical integration is not possible, at least for non-trivial initial vortex shapes. On the other hand, its numerical integration gives at any time $t > 0$ only a finite set of points, from which an approximate vortex boundary can be rebuilt. Nothing is known about the analytical properties of $\partial P(t)$: *there is no way* (at least, to the author's knowledge) *to define the Schwarz function of this curve*. As a consequence, almost all the analytical investigations about the dynamics in the literature (see e.g. [12–15] among many others) concern (rotating) equilibria, in which the shape of the vortex is retained. The studies in which it really changes are confined to small departures from circular or elliptical shapes [16–18], essentially due to convergence problems in the series representations of the solutions.

The present paper adopts a rather different point of view. Instead of working on the contour dynamics problem (1), in case with the aid of the new kinematic relation (2), this latter relation is used to deduce a new evolution equation for the Schwarz function. In this way, the analysis is directly focused on the time evolution of the vortex shape, overcoming any difficulty in identifying $\boldsymbol{\Phi}$ from a finite set of points. The equation for $\boldsymbol{\Phi}$ is integrodifferential, singular (contains an integral that must be evaluated in its principal value) and strongly nonlinear. However, it possesses an attractive structure: its nonlinearity is confined inside a single term. This property opens the way to estimate its (analytical) solution through the method of successive approximations (see [19] page 84, or [20] pages 5, 49), which leads to a hierarchy of linear equations. The 0th order equation takes the nonlinear term as zero, while in the kth one ($k = 1, 2, \ldots$), the nonlinear term is assumed as a forcing one and evaluated in correspondence with the available $(k-1)$th solution. Due to the fact that its complexity quickly grows for increasing k, the present analysis is confined to the first-order equation.

The paper is organized as follows. The evolution equation for the Schwarz function is derived in Sect. 2 together with the hierarchy of linear singular equations. The 0th-and 1st-order solutions are then calculated by solving the corresponding equations in Sect. 3. In Sect. 4, they are specified for a certain class of vortices,

[1] An extensive theoretical background on the Schwarz function can be found in [10].

the kinematics of which has been recently investigated [11]. Several important issues about these solutions are discussed in Sect. 5, while in Sect. 6, they are compared with the numerical simulations. Finally, conclusions are offered in Sect. 7 together with a plan of future researches.

2 An integral approach to the self-induced dynamics

In the present section, an equation describing the evolution in time of the Schwarz function of the vortex boundary is proposed. It is integral, singular and strongly nonlinear. Although it is not aimed at replacing the classical contour dynamics problem (1) in order to numerically integrate the vortex motion, it provides powerful tools to analytically investigate some interesting features of the dynamics. A convenient analytical approximation of its solution is also proposed.

In order to avoid convective terms, a Lagrangian description of the vortex motion is here adopted. To this aim, the analytic function $\boldsymbol{S}$ depending on the position $\boldsymbol{\xi}$ at the reference time ($t = 0$) and on the time t is introduced. It is defined by means of the analytic continuation of its values on $\partial P(0)$, which are assigned according to the relation: $\boldsymbol{S}(\boldsymbol{\xi}; t) = \boldsymbol{\Phi}[\boldsymbol{x}(\boldsymbol{\xi}; t); t]$ in any $\boldsymbol{\xi} \in \partial P(0)$. It is worth remarking that $\boldsymbol{S}(\boldsymbol{\xi}; t)$ is different from $\boldsymbol{\Phi}[\boldsymbol{x}(\boldsymbol{\xi}; t); t]$ outside $\partial P(0)$, the flow $\boldsymbol{x}(\boldsymbol{\xi}; t)$ being a non-analytic function of the position $\boldsymbol{\xi}$. Nevertheless, in the following, $\boldsymbol{S}$ will be called *Lagrangian Schwarz function* of the curve ∂P.

The definition of $\boldsymbol{S}$ implies $\boldsymbol{S}(\boldsymbol{\xi}; t) = \overline{\boldsymbol{x}}(\boldsymbol{\xi}; t)$ in any $\boldsymbol{\xi} \in \partial P(0)$. By deriving in time both sides of the above relation, the evolution equation of $\boldsymbol{S}$:

$$\partial_t \boldsymbol{S}(\boldsymbol{\xi}; t) = \overline{\boldsymbol{u}}[\boldsymbol{x}(\boldsymbol{\xi}; t); t] \tag{3}$$

follows. It is valid on $\partial P(0)$ only. However, if the conjugate velocity at its right-hand side is replaced by the analytic continuation of the function $\overline{\boldsymbol{u}}[\boldsymbol{x}(\boldsymbol{\xi}; t); t]$, it becomes valid on a suitable neighbourhood of $\partial P(0)$.

It is now interesting to use Eq. (3) in deducing Kirchhoff's solution for a uniform elliptical vortex. To this aim, its Eulerian analytic continuation is introduced:

$$\partial_t \boldsymbol{\Phi}(\boldsymbol{x}; t) + \boldsymbol{U}(\boldsymbol{x}; t)\partial_{\boldsymbol{x}} \boldsymbol{\Phi}(\boldsymbol{x}; t) = \overline{\boldsymbol{U}}(\boldsymbol{x}; t), \tag{4}$$

$\boldsymbol{x}$ lying in a suitable neighbourhood of $\partial P(t)$. In the above equation, $\boldsymbol{U}$ and $\overline{\boldsymbol{U}}$ (here the bar is just a symbol) are the analytic continuations of the velocity $\boldsymbol{u}$ and of its conjugate $\overline{\boldsymbol{u}}$ on the vortex boundary. $\overline{\boldsymbol{U}}$ is different from $\overline{\boldsymbol{u}}$ inside the vortex (where $\overline{\boldsymbol{U}}$ is analytic and $\overline{\boldsymbol{u}}$ is not), while $\boldsymbol{U}$ is different from $\boldsymbol{u}$ everywhere. It is worth stressing that, at least in general, the use of the dynamics (4) is not easy, $\boldsymbol{U}$ being related to the Schwarz function in a very involved way. Nevertheless, it will be now employed in studying the motion of a uniform elliptical vortex.

The vortex has its centre of vorticity on the origin. The lengths of its semi-axes are a and b ($a > b$), the first one forming the angle α with respect to the positive real axis. As is well known, Kirchhoff's solution states that the vortex boundary rotates at the constant velocity $\Omega = \omega ab/(a+b)^2$, without deforming. This solution is now recovered by using Eq. (4). As a matter of fact, the Schwarz function of the vortex boundary is given as

$$\boldsymbol{\Phi}(\boldsymbol{x}; t) = \underbrace{\frac{a^2+b^2}{\boldsymbol{c}^2}}_{\boldsymbol{\mu}_1} \boldsymbol{x} - \underbrace{\frac{2ab}{\boldsymbol{c}^2}}_{\boldsymbol{\mu}_2} (\boldsymbol{x}^2 - \underbrace{\boldsymbol{c}^2}_{\boldsymbol{\mu}_3})^{1/2}, \tag{5}$$

where $\boldsymbol{c}$ is a focus position, that is, $\boldsymbol{c} := c\exp(\boldsymbol{i}\alpha)$ with $c = \sqrt{a^2 - b^2}$, and the functions of time $\boldsymbol{\mu}_{1,2,3}$ are introduced here for later convenience. Moreover, an application of Eq. (2) leads to the analytic continuations of velocity and conjugate velocity:

$$\overline{\boldsymbol{U}}(\boldsymbol{x}; t) = \boldsymbol{i}\frac{\omega ab}{\boldsymbol{c}^2}\left(-\boldsymbol{x} + \sqrt{\boldsymbol{x}^2 - \boldsymbol{c}^2}\right), \quad \boldsymbol{U}(\boldsymbol{x}; t) = \boldsymbol{i}\frac{\omega ab}{(a+b)^2}\left(\boldsymbol{x} + \sqrt{\boldsymbol{x}^2 - \boldsymbol{c}^2}\right). \tag{6}$$

Assume now that *the algebraic structure of the Schwarz function* (5) *is retained during the motion* and that a, b and $\boldsymbol{c}$ depend on time. By inserting the functions (5, 6) in the dynamics (4), one easily obtains $\dot{a} = \dot{b} = 0$ and $\dot{\boldsymbol{c}} = \boldsymbol{i}\Omega\boldsymbol{c}$, that is, the aforementioned Kirchhoff's solution.

Coming back to the general case, the conjugate velocity on the current vortex boundary $\partial P(t)$ can be written in terms of a Cauchy integral in the Schwarz function (2), as discussed in Sect. 1. By inserting in

Eq. (3) this integral form of $\overline{\boldsymbol{u}}$ and changing the variables from Eulerian to Lagrangian ones, the following integrodifferential problem [2] is deduced:

$$\begin{cases} \partial_\tau \boldsymbol{S}(\boldsymbol{\xi};\tau) = -\boldsymbol{i}\left[\boldsymbol{S}(\boldsymbol{\xi};\tau) - \dfrac{1}{\pi \boldsymbol{i}} \fint_{\partial P(0)} \mathrm{d}\boldsymbol{\eta} \dfrac{\boldsymbol{S}(\boldsymbol{\eta};\tau)}{\boldsymbol{\eta}-\boldsymbol{\xi}} - \dfrac{1}{\pi \boldsymbol{i}} \displaystyle\int_{\partial P(0)} \mathrm{d}\boldsymbol{\eta}\, \boldsymbol{g}(\boldsymbol{\eta},\boldsymbol{\xi};\tau)\boldsymbol{S}(\boldsymbol{\eta};\tau)\right] \\ \boldsymbol{S}(\boldsymbol{\xi};0) = \boldsymbol{S}_0(\boldsymbol{\xi}) \quad \text{(given)}. \end{cases} \tag{7}$$

In the problem (7), the non-dimensional time $\tau = t\omega/4$ has been used (it gives an eddy turnover time π for a Rankine vortex and slightly larger rotation periods for non-circular ones). Moreover, the nonlinearity is confined in the last term, which depends on the displacement ratio $\boldsymbol{h}(\boldsymbol{\eta},\boldsymbol{\xi};\tau) := [\boldsymbol{x}(\boldsymbol{\eta};\tau) - \boldsymbol{x}(\boldsymbol{\xi};\tau)]/(\boldsymbol{\eta}-\boldsymbol{\xi})$ by means of the function $\boldsymbol{g} := \partial_\eta \log \boldsymbol{h}$. It is worth remarking that this term vanishes at the initial time, due to the fact that $\boldsymbol{h}(\boldsymbol{\eta},\boldsymbol{\xi};0) \equiv 1$ and then $\boldsymbol{g}(\boldsymbol{\eta},\boldsymbol{\xi};0) \equiv 0$.

More complicated flows can also be investigated by using the above approach. For example, in the presence of strain [21], the term $\boldsymbol{i}\gamma_s \boldsymbol{x} \exp(-2\boldsymbol{i}\varphi_s)$ has to be added to the right-hand side of Eq. (3), γ_s and φ_s being the (time-dependent) intensity and orientation of the strain field. Once this term is changed in $\boldsymbol{i}\gamma_s \boldsymbol{\xi} \exp(-2\boldsymbol{i}\varphi_s) + \boldsymbol{i}\gamma_s(\boldsymbol{x}-\boldsymbol{\xi}) \exp(-2\boldsymbol{i}\varphi_s)$, the present approach can be easily extended. Indeed, the first term is known and the second one is nonlinear and vanishes at the initial time.

As stated in Sect. 1, the initial value problem (7) is here proposed with the aim to investigate the vortex motion in an analytical fashion. From this point of view, it appears more useful than the classical contour dynamics one (1). As a matter of fact, the problem (7) focuses on the time evolution of the vortex shape, being written in the corresponding Schwarz function. On the contrary, there is no way to understand the role of the shape in the problem (1). This is a rather subtle consequence of the still unresolved difficulty in identifying the Schwarz function of the curve $\partial P(t)$, as it follows from the numerical integration of the contour dynamics problem at $t > 0$.

The integrodifferential problem (7) is now transformed into an integral equation by means of the Laplace transform in time (the conjugate variable of τ is called $\boldsymbol{\sigma}$):

$$\underbrace{(\boldsymbol{i}\boldsymbol{\sigma}-1)\tilde{\boldsymbol{S}}(\boldsymbol{\xi};\boldsymbol{\sigma}) + \frac{1}{\pi \boldsymbol{i}} \fint_{\partial P(0)} \mathrm{d}\boldsymbol{\eta} \frac{\tilde{\boldsymbol{S}}(\boldsymbol{\eta};\boldsymbol{\sigma})}{\boldsymbol{\eta}-\boldsymbol{\xi}}}_{\mathbf{SD}[\tilde{\boldsymbol{S}}]\text{:singular dominant term}} + \underbrace{\frac{1}{\pi \boldsymbol{i}} \int_{\partial P(0)} \mathrm{d}\boldsymbol{\eta}\, \widetilde{\boldsymbol{g}\boldsymbol{S}}(\boldsymbol{\eta},\boldsymbol{\xi};\boldsymbol{\sigma})}_{\mathbf{R}[\tilde{\boldsymbol{S}}]\text{:regular term}} = \underbrace{\boldsymbol{i}\boldsymbol{S}_0(\boldsymbol{\xi})}_{\mathbf{ID}[\tilde{\boldsymbol{S}}]\text{:data}}, \tag{8}$$

$\tilde{\boldsymbol{S}}$ being the transform of $\boldsymbol{S}$. In the above equation, the singular contribution is linear, while the regular one is strongly nonlinear, due to the presence of the function $\boldsymbol{g}$.

An attempt to analytically approximate the solution of the Eq. (8) is now explored. It is based on the structure of the above equation, in which the nonlinearity is confined inside the regular term $\mathbf{R}$, only. This attractive feature suggests to build a hierarchy of linear singular integral equations by using the method of the successive approximations, as is usually done for nonlinear integral equations. It is worth remarking that the present approach is different from other analytical ones, which employ truncated Laurent series representations of the solution in order to capture the deformations about a basic shape (circular or elliptical). In these approaches, the departures from the fixed vortex geometry must be small, in order to ensure the convergence of the series. Moreover, the algebraic structure of the approximate solution cannot be easily understood, being given by the sum of a series. The present method does not require the deformations to be small, it does not perform any linearization, and at least in principle, it leads to the algebraic structure of the approximate solution. The only difficulty that is experienced lies in the algebraic complexity of the solutions, which quickly grows with the order of the approximation.

The hierarchy of the linear approximating equations is built as follows. Equation (8) is first rewritten by keeping $\mathbf{R} = 0$ also for $t > 0$:

$$\mathbf{SD}[\tilde{\boldsymbol{S}}^{(0)}] = \mathbf{ID} =: \boldsymbol{H}^{(0)}. \tag{9}$$

Once the above linear equation has been solved, the 0th order approximation of the Schwarz function $\boldsymbol{S}^{(0)}$ follows. This approximation is then employed to compute a less rough estimate of the regular term,

[2] The bar superimposed to the integral symbol means that it is evaluated in its Cauchy principal value.

by evaluating $\mathbf{R}$ in correspondence with $\tilde{\boldsymbol{S}}^{(0)}$. This approximation of the regular term, that is, $\mathbf{R}[\tilde{\boldsymbol{S}}^{(0)}]$, is then viewed as a forcing term for the first-order problem, which is formulated as follows:

$$\mathbf{SD}[\tilde{\boldsymbol{S}}^{(1)}] = \mathbf{ID} - \mathbf{R}[\tilde{\boldsymbol{S}}^{(0)}] =: \boldsymbol{H}^{(1)}. \tag{10}$$

By solving this equation, a better approximation ($\boldsymbol{S}^{(1)}$) of the Schwarz function is obtained, and so on. However, the successive approximations are truncated at the 1st order in the present paper, due to the complicated algebraic structure of the nonlinear regular term $\mathbf{R}[\tilde{\boldsymbol{S}}^{(0)}]$. Despite a mathematical proof of the convergence of the successive approximations to the solution of the problem (7) is still lacking, $\boldsymbol{S}^{(1)}$ (10) is expected to be closer to the solution of the problem (7) than $\boldsymbol{S}^{(0)}$ (9). In Sect. 6, the comparison with contour dynamics simulations will give an experimental proof of this important conjecture.

Finally, the singular integral equations (9, 10) are solved once for all by using standard techniques [22], and the following Laplace transform of the kth ($k = 0, 1$) approximation of the Schwarz function in any point $\boldsymbol{\xi} \in \partial P(0)$:

$$\tilde{\boldsymbol{S}}^{(k)}(\boldsymbol{\xi}; \boldsymbol{\sigma}) = -\frac{\boldsymbol{i}\boldsymbol{\sigma} - 1}{\boldsymbol{\sigma}(\boldsymbol{\sigma} + 2\boldsymbol{i})}\boldsymbol{H}^{(k)}(\boldsymbol{\xi}; \boldsymbol{\sigma}) + \frac{1}{\boldsymbol{\sigma}(\boldsymbol{\sigma} + 2\boldsymbol{i})}\frac{1}{\pi\boldsymbol{i}} \fint_{\partial P(0)} \mathrm{d}\boldsymbol{\eta} \frac{\boldsymbol{H}^{(k)}(\boldsymbol{\eta}; \boldsymbol{\sigma})}{\boldsymbol{\eta} - \boldsymbol{\xi}} \tag{11}$$

is obtained. The Laplace antitransforms of the above solutions are evaluated in the next section.

3 Approximate solutions at zero and first orders

In the 0th order problem (9), $\boldsymbol{H}^{(0)}$ is simply given by $\boldsymbol{i}\boldsymbol{S}_0$, for any $\boldsymbol{\sigma}$. The Laplace antitransform of the corresponding solution (11), evaluated by using the result (23) of Appendix A, leads to the definition of the 0th order Schwarz function in any point $\boldsymbol{\xi}$ on the initial boundary:

$$\boldsymbol{S}^{(0)}(\boldsymbol{\xi}; \tau) = \boldsymbol{S}_0(\boldsymbol{\xi}) + \frac{1}{2\boldsymbol{i}}\frac{\boldsymbol{\tau}}{1 + \boldsymbol{\tau}}\overline{\boldsymbol{u}}_0(\boldsymbol{\xi}), \tag{12}$$

$\boldsymbol{\tau} = \exp(2\boldsymbol{i}\tau) - 1$ being the "complexified" time and $\overline{\boldsymbol{u}}_0(\boldsymbol{\xi})$ the conjugate velocity $\overline{\boldsymbol{u}}[\boldsymbol{\xi}, \boldsymbol{S}_0(\boldsymbol{\xi}); 0]$ (divided by $\omega/4$). The solution (12) is periodic in time with period[3] $T = 4\pi/\omega$.

Once the Schwarz function on $\partial P(0)$ is known, its conjugate gives the 0th order position as:

$$\boldsymbol{x}^{(0)}(\boldsymbol{\xi}; \tau) = \boldsymbol{\xi} + \frac{\boldsymbol{\tau}}{2\boldsymbol{i}}\boldsymbol{u}_0(\boldsymbol{\xi}). \tag{13}$$

As $\boldsymbol{\xi}$ runs on $\partial P(0)$, the point $\boldsymbol{x}^{(0)}(\boldsymbol{\xi}; \tau)$ (13) moves on the 0th order approximation of the boundary at time τ, called $\partial P^{(0)}(\tau)$ hereafter. The behaviour in time of this approximation is discussed in Sect. 6, where it is evaluated in correspondence with sample vortices. In general, $\partial P^{(0)}$ agrees in a quite unsatisfactory way with the true boundary, obtained by means of an accurate contour dynamics simulation. Nevertheless, it is very important from a theoretical point of view, in order to calculate the next approximation ($\partial P^{(1)}$) of the boundary and also for reasons that will be discussed in Sect. 7.

As a sample case, the 0th order solution (12) is now evaluated for a uniform elliptical vortex. Due to the fact that it is periodic with period π, while the vortex rotates with a different (and shape-dependent) period, Kirchhoff's solution cannot be recovered. However, it is interesting to compare the true Schwarz function (5) and the present 0th order one. It has the same algebraic structure, but with the following coefficients:

$$\boldsymbol{\mu}^{(0)}_{1,2}(\tau) = \frac{c^2}{2\left[(a-b)^2 + 4ab\mathrm{e}^{2\boldsymbol{i}\tau}\right]} \pm \frac{4ab + (a-b)^2\mathrm{e}^{2\boldsymbol{i}\tau}}{2c^2\mathrm{e}^{2\boldsymbol{i}\tau}}, \quad \boldsymbol{\mu}^{(0)}_3(\tau) = \frac{a-b}{a+b}\left[(a-b)^2 + 4ab\mathrm{e}^{2\boldsymbol{i}\tau}\right].$$

The above coefficients are compared with the true ones in Fig. 1 for small (first row) and large (second) eccentricities ($\varepsilon := c/a$). It is worth noticing that for small ε, the agreement appears to be very satisfactory. On the contrary, for increasing ε, the errors $\boldsymbol{\mu}_k - \boldsymbol{\mu}^{(0)}_k$ ($k = 1, 2$ and 3) become larger and the 0th order approximation quite poor.

[3] It agrees with the one of the Kirchhoff solution [7] for an elliptical vortex. Indeed, the period of rotation of the elliptical vortex boundary is given by $T_e = 2\pi(a+b)^2/(\omega ab) \simeq 2T$, a and b being the semi-axes. Due to the fact that the motion of the material particles inside the vortex is periodic with period $T_e/2$, $\boldsymbol{S}^{(0)}$ changes with a period close to T.

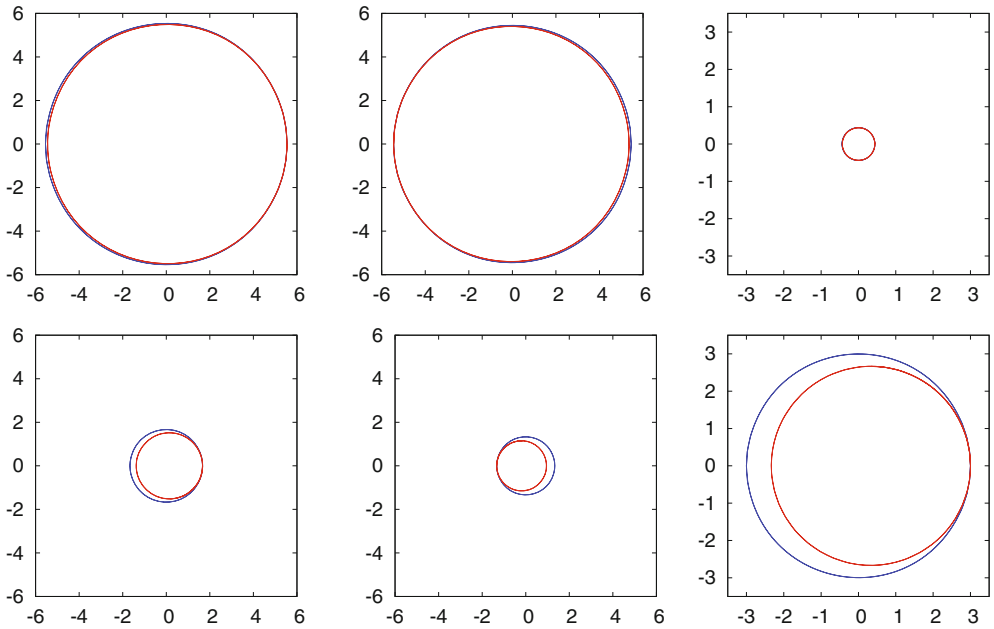

Fig. 1 Coefficients $\boldsymbol{\mu}_k$ in Eq. (5) (*blue lines*) and $\boldsymbol{\mu}_k^{(0)}$ *(red)* for $k = 1$ (first column), 2 (second) and 3 (third) during a period of rotation of the vortex. b is 1, while a is 1.2 ($\varepsilon \simeq 0.553$) in the first row and 2 ($\varepsilon \simeq 0.866$) in the second one

The first-order solution $\boldsymbol{S}^{(1)}$ is now deduced. Its Laplace transform follows from the general form (11) of the solution, once the right-hand side $\boldsymbol{H}^{(1)}$ of Eq. (10) has been calculated. To this aim, the regular term $\mathbf{R}$ is evaluated in correspondence with the solution (12,13), by introducing the following function:

$$\boldsymbol{N}(\boldsymbol{\xi};\tau) := \frac{1}{\pi \boldsymbol{i}} \int\limits_{\partial P(0)} \mathrm{d} \log \boldsymbol{h}^{(0)}(\boldsymbol{\eta},\boldsymbol{\xi};\tau)\boldsymbol{S}^{(0)}(\boldsymbol{\eta};\tau), \tag{14}$$

the Laplace transform of which just gives $\mathbf{R}[\tilde{\boldsymbol{S}}^{(0)}]$. In the above definition, $\boldsymbol{h}^{(0)}$ is the 0th order displacement ratio $[\boldsymbol{x}^{(0)}(\boldsymbol{\eta};\tau) - \boldsymbol{x}^{(0)}(\boldsymbol{\xi};\tau)]/(\boldsymbol{\eta} - \boldsymbol{\xi})$. From the formula (14), it follows that $\boldsymbol{N}$ depends on the roots of the equation in $\boldsymbol{\eta}$: $\boldsymbol{x}^{(0)}(\boldsymbol{\eta};\tau) = \boldsymbol{x}^{(0)}(\boldsymbol{\xi};\tau)$ different from $\boldsymbol{\xi}$, as it will be discussed in the next section.

Moreover, the calculation of the above nonlinear term must also take into account the topology of $\partial P^{(0)}$. As a matter of fact, the part of $\boldsymbol{N}$ containing the differential $\mathrm{d}\boldsymbol{x}^{(0)}(\boldsymbol{\eta};\tau)$ can be viewed as evaluated on the curve $\partial P^{(0)}$ (oriented in a counterclockwise sense), so that it changes if this curve is simple or not. In the first case, a straightforward application of the residue theorem leads to the value of $\boldsymbol{N}$. In the second one, $\partial P^{(0)}(\tau)$ is the union of two simple and closed curves on which $\boldsymbol{x}^{(0)}(\boldsymbol{\eta};\tau)$ moves in opposite directions as $\boldsymbol{\eta}$ runs counterclockwise on $\partial P(0)$. As a consequence, the domain of integration $\partial P(0)$ in Eq. (14) must be split in two *open* arcs and the corresponding integrals have to be evaluated in a different way.

The 1st-order solution $\tilde{\boldsymbol{S}}^{(1)}$ (11) is computed by using the Laplace transform of the function (14). Its Laplace antitransform is evaluated through convolutions in time, as discussed in Appendix A. It follows the 1st-order Lagrangian Schwarz function:

$$\begin{aligned}\boldsymbol{S}^{(1)}(\boldsymbol{\xi};\tau) = \boldsymbol{S}^{(0)}(\boldsymbol{\xi};\tau) + \frac{\boldsymbol{i}}{2}\Bigg\{ &\int_0^\tau \mathrm{d}\tau' [\,1 + \mathrm{e}^{-2\boldsymbol{i}(\tau-\tau')}\,]\,\boldsymbol{N}(\boldsymbol{\xi};\tau') \\ &+ \frac{1}{\pi \boldsymbol{i}} \int\limits_{\partial P(0)} \frac{\mathrm{d}\boldsymbol{\eta}}{\boldsymbol{\eta} - \boldsymbol{\xi}} \int_0^\tau \mathrm{d}\tau' [\,1 - \mathrm{e}^{-2\boldsymbol{i}(\tau-\tau')}\,]\,\boldsymbol{N}(\boldsymbol{\eta};\tau') \Bigg\},\end{aligned} \tag{15}$$

in any point $\boldsymbol{\xi}$ on $\partial P(0)$. By conjugating the above function, the 1st-order approximation $\partial P^{(1)}$ of the vortex boundary is also obtained. As will be discussed below, it behaves in a quite satisfactory way even at times

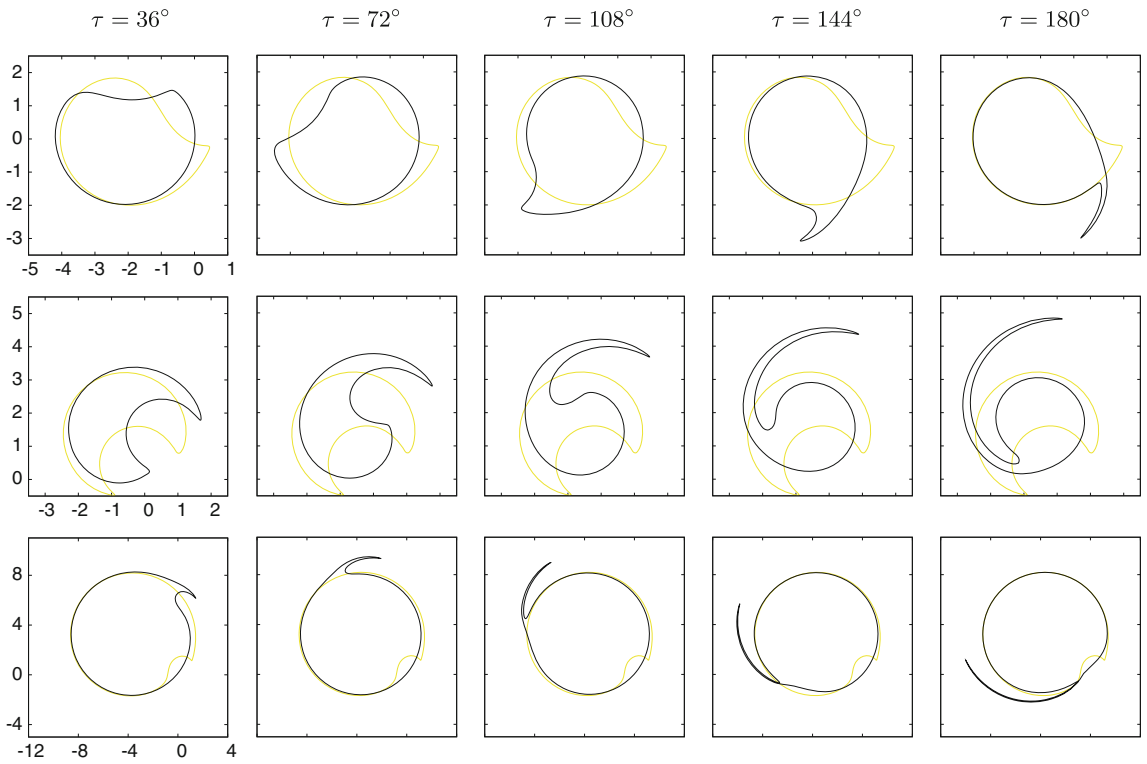

Fig. 2 Vortex boundaries (*black lines*) at different times (indicated above, in sexagesimal degrees), obtained by means of contour dynamics simulations. The initial Schwarz functions have the form (16), with $a_1 = 1$ and: $a_2 = 0.2 + i$, $z_1 = -0.7 + 0.05i$, $z_2 = -1 + 1.5i$ (first row); $a_2 = 0.8 - 0.2i$, $z_1 = 0.6 - 1.1i$, $z_2 = -0.1 + 0.3i$ (second); $a_2 = 0.5 - 0.1i$, $z_1 = 0.8 - 0.75i$, $z_2 = 0.4 + 0.2i$ (third). The initial vortex boundaries (*yellow lines*) are also drawn. The simulations are performed with relative errors on circulation and second-order moment smaller than $2 \cdot 10^{-4}$

in which $\partial P^{(0)}$ is non-simple. For this reason, its calculation in correspondence with sample vortices will be discussed in some details.

The 0th- and 1st-order solutions (12,15) are now used for investigating the dynamics of vortices the boundaries of which possess Schwarz functions of simple forms.

4 First-order solution for a class of sample vortices

The 1st-order Schwarz function (15) is now specified for vortices the Schwarz functions of which possess two simple poles in a transformed z-plane [11], the corresponding self-induced velocities being analytically known. Samples of the dynamics of this kind of vortices are shown in Fig. 2. Before discussing this application, a short overview of the kinematics of this kind of vortices is here offered.

The Schwarz function at the initial time is assumed in the following form:

$$S_0[\xi(z)] := \overline{\xi}(z) = \frac{a_1}{z - z_1} + \frac{a_2}{z - z_2}, \tag{16}$$

where z runs on the unit circle $\mathcal{C}$ (hereafter, z and ζ will be used for the images of ξ and η in the plane of the circle). Introduced the image points $w_{1,2} = 1/\overline{z}_{1,2}$, residues and poles of S_0 will appear often combined into the constants $\alpha := \overline{a}_1 w_1^2 + \overline{a}_2 w_2^2$, $\beta := w_1 w_2 (\overline{a}_1 w_1 + \overline{a}_2 w_2)$ and $\gamma := w_1^2 w_2^2 (\overline{a}_1 + \overline{a}_2)$.

The initial vortex shape follows by conjugating the function (16):

$$\xi(z) = -\frac{\overline{a}_1 w_1^2}{z - w_1} - \frac{\overline{a}_2 w_2^2}{z - w_2} - \frac{\beta}{w_1 w_2}, \tag{17}$$

having used the fact that z lies on $\mathcal{C}$ (i.e. $\overline{z} = 1/z$).

In order to evaluate the Schwarz function $\boldsymbol{S}_0$ or the corresponding self-induced conjugate velocity $\overline{\boldsymbol{u}}_0$ *outside* the vortex boundary, the analytic continuation of the function (17) *outside* the unit circle is needed. It follows from the above definition of $\boldsymbol{\xi}$ in the natural way, even if its domain D_0 (and also its range R_0, as it will be shown below) of this map must be still identified. At the present stage, the only known properties of D_0 and R_0 are that D_0 includes $\mathcal{C}$ and R_0 covers almost all the physical plane. It is shown in [11] that the calculation of the inverse function $z = z(\boldsymbol{\xi})$ leads also to the definition of D_0 and R_0. The main steps of this calculation can be summarized as follows.

First, it is worth remarking that the equation in $\boldsymbol{\zeta}$: $\boldsymbol{\eta}(\boldsymbol{\zeta}) = \boldsymbol{\xi}(z)$ possesses two roots, the trivial one ($\boldsymbol{\zeta} = z$) and the root:

$$\boldsymbol{\zeta} = \boldsymbol{\zeta}^\star(z) = \frac{\boldsymbol{\beta} z - \boldsymbol{\gamma}}{\boldsymbol{\alpha} z - \boldsymbol{\beta}}. \tag{18}$$

Due to the fact that the function (17) maps the points z and $\boldsymbol{\zeta}^\star(z)$ on the same $\boldsymbol{\xi}$, the function (18) will be also named as the *pseudo-inverse* of the function (17), even if it acts on z and not on $\boldsymbol{\xi}$. A second important issue concerns the requirement that the vortex boundary is a simple curve, or equivalently that the circle $\boldsymbol{\zeta}^\star(\mathcal{C}) =: \mathcal{C}^\star$ does not intersect $\mathcal{C}$. It leads to constraints on residues and poles of the Schwarz function (16). A classification based on the relative positions of $\mathcal{C}^\star$ with respect to $\mathcal{C}$ and on the properties of the map $z \mapsto \boldsymbol{\xi}$ (17) is also introduced, in order to separate vortices having different kinematic properties.

The analysis of the pseudo-inverse map (18) shows that a one-parameter family of circles $\{\mathcal{C}_i(\mu)$, with μ real$\}$ exists such that any circle of the family results to be an *invariant* curve for the function $\boldsymbol{\zeta}^\star$, that is, $\boldsymbol{\zeta}^\star(\mathcal{C}_i) = \mathcal{C}_i$. Furthermore, any $\mathcal{C}_i$ is mapped by the function (17) onto an arc of circle $\tilde{\mathcal{C}}_i$ in the physical plane: as z runs on $\mathcal{C}_i$, the point $\boldsymbol{\xi}(z)$ moves on that arc first in a direction and then in the reverse one. All the circles of the above family intersect on the two fixed points $z_{io}^{\mp}$ of the map (18), which are transformed by the function (17) in the endpoints $\boldsymbol{\xi}_{io}^{\mp}$ of the arc $\tilde{\mathcal{C}}_i$. As μ changes, different arcs $\tilde{\mathcal{C}}_i$ are obtained, despite their endpoints remaining fixed.

Any circle $\mathcal{C}_i$ divides the z-plane in two regions that are mapped one to the other one by the pseudo-inverse function (18). The unit circle lies in one of them, which, therefore, is the domain D_0 of the map (17). Its range R_0 is the plane cut[4] along the arc $\tilde{\mathcal{C}}_i$. In other words, the inverse map $\boldsymbol{\xi} \mapsto z$ is defined almost everywhere in the physical plane, its limit values from the two sides of $\tilde{\mathcal{C}}_i$ leading to different points on $\mathcal{C}_i$. As a final remark, note that any choice of μ leads to different branches of the function $z \mapsto \boldsymbol{\xi}$ (17) and of its inverse $\boldsymbol{\xi} \mapsto z$.

In the present paper, the first-order solution (15) is evaluated for three sample vortices, the dynamics of which is shown in the three rows of Fig. 2. Despite these vortices are of different kinds with respect to the classification in [11], they possess the same algebraic structure of the self-induced velocity $\boldsymbol{u}_0$:

$$\boldsymbol{u}_0[\boldsymbol{\xi}(z)] = \frac{\boldsymbol{b}_1}{z - \boldsymbol{w}_1} + \frac{\boldsymbol{b}_2^\star}{z - \boldsymbol{w}_2^\star} + \boldsymbol{b}_0, \tag{19}$$

in which $\boldsymbol{w}_2^\star = 1/\overline{z}_2^\star$ with $z_2^\star := \boldsymbol{\zeta}^\star(z_2)$. The coefficients $\boldsymbol{b}_0$, $\boldsymbol{b}_1$ and $\boldsymbol{b}_2^\star$ depend on poles and residues of the Schwarz function (16). In order to calculate the nonlinear term $\boldsymbol{N}$, the 0th order displacement ratio $\boldsymbol{h}^{(0)}$ is specified in terms of the initial shape (17) and velocity (19):

$$\boldsymbol{h}^{(0)}[\boldsymbol{\eta}(\boldsymbol{\zeta}), \boldsymbol{\xi}(z); \tau] = \frac{\boldsymbol{P}(z; \boldsymbol{\tau} \mid \boldsymbol{\zeta})}{(z - \boldsymbol{\zeta}_\infty^\star)(z - \boldsymbol{w}_2^\star)(\boldsymbol{\zeta} - \boldsymbol{w}_2^\star)[\boldsymbol{\zeta} - \boldsymbol{\zeta}^\star(z)]}. \tag{20}$$

In the above formula, $\boldsymbol{\zeta}_\infty^\star$ stays for $\boldsymbol{\zeta}^\star(\infty) = \boldsymbol{\beta}/\boldsymbol{\alpha}$ and $\boldsymbol{P}$ is a polynomial which is quadratic in $\boldsymbol{\zeta}$ and z and linear in $\boldsymbol{\tau}$. Due to the symmetry of $\boldsymbol{h}^{(0)}$ with respect to $\boldsymbol{\eta}$ and $\boldsymbol{\xi}$, $\boldsymbol{P}$ is also symmetric in z and $\boldsymbol{\zeta}$. Its roots in $\boldsymbol{\zeta}$ are named as $\boldsymbol{F}_\mp$ (the sign $+$ indicates that the principal branch of the square root of the discriminant is used, while $-$ refers to the secondary one) and depend on z and on τ. As functions of z, they possess four time-dependent branch points $\tilde{z}_1, \ldots, \tilde{z}_4$. Finally, the polynomial $\boldsymbol{P}$ together with its roots verifies the following property:

$$\boldsymbol{P}[\boldsymbol{F}_+(z; \tau); \boldsymbol{\tau} \mid \boldsymbol{F}_-(z; \tau)] \equiv 0 \tag{21}$$

[4] In all the sample vortices investigated in the present paper (of kinds (1, 1), (2, 2) and (3, 2) [11]), the value of μ can be selected in such a way that the cut $\tilde{\mathcal{C}}_i$ lies inside the vortex.

for any z and τ. The identity (21) means that $\boldsymbol{P}$ vanishes when its coefficients are calculated in one root and the polynomial in the other one: it is called *reciprocity*.

Once $\boldsymbol{h}^{(0)}$ has been evaluated, the nonlinear term (14) follows at times in which $\partial P^{(0)}$ is a simple curve as:

$$\boldsymbol{N} = \frac{1}{\pi \boldsymbol{i}} \int_{\mathcal{C}} \mathrm{d}\boldsymbol{\zeta} \left(\frac{1}{\boldsymbol{\zeta} - \boldsymbol{F}_-} + \frac{1}{\boldsymbol{\zeta} - \boldsymbol{F}_+} - \frac{1}{\boldsymbol{\zeta} - \boldsymbol{w}_2^\star} - \frac{1}{\boldsymbol{\zeta} - \boldsymbol{\zeta}^\star} \right) \times \left[\frac{\boldsymbol{a}_2}{\boldsymbol{\zeta} - z_2} + \frac{1}{\boldsymbol{\tau} + 1} \left(\frac{\boldsymbol{a}_1}{\boldsymbol{\zeta} - z_1} + \frac{\boldsymbol{\tau} \boldsymbol{c}_2^\star}{\boldsymbol{\zeta} - z_2^\star} + \boldsymbol{\tau} \boldsymbol{c}_0 \right) \right],$$

where $\boldsymbol{c}_2^\star$ and $\boldsymbol{c}_0$ are coefficients depending on poles and residues of the Schwarz function (16). If $\partial P^{(0)}$ is not a simple curve, $\boldsymbol{N}$ assumes a more complicated form, still depending on the roots $\boldsymbol{F}_\mp$. In both cases, the nonlinear term can be analytically evaluated only if the relative positions between $\boldsymbol{F}_\mp$ and $\mathcal{C}$ are known. For this reason, a preliminary analysis of the behaviour of the roots $\boldsymbol{F}_\mp$ as functions of time and space is needed. It is briefly summarized in the next section, before discussing the numerical results of the present approach. For the sake of shortness, the analysis is here confined to the vortex in the first row of Fig. 2.

5 Behaviour of the maps $\boldsymbol{F}_\mp$

It is worth remembering that these functions depend on the positions of four branch points $\tilde{z}_1, \ldots, \tilde{z}_4$, which in turn change in time. In Appendix B, the motion of these points is briefly investigated, by showing that two of them run on large trajectories and intersect $\mathcal{C}$ at certain times $\tau_{2,3}^\star$ (see Fig. 9 in Appendix C), while the other two points move in small neighbourhoods of their initial positions.

A convenient way to begin the study of the functions $\boldsymbol{F}_\mp$ during an eddy turnover time consists in considering their action on $\mathcal{C}$. The unit circle is transformed into the time-dependent curves $\mathcal{L}_\mp := \boldsymbol{F}_\mp(\mathcal{C})$, which play a special role in the 1st-order solution $\boldsymbol{S}^{(1)}$ (15). In fact the nonlinear term $\boldsymbol{N}$ (14) depends on their relative positions with respect to $\mathcal{C}$.

These curves are drawn in Fig. 3 at several times during an eddy turnover period.

A quick look at these pictures leads to the identification of another couple of important times, at which $\mathcal{L}_-$ touches $\mathcal{C}$ and simultaneously a cusp appears or disappears on $\mathcal{L}_+$. These times are named as $\tau_{1,4}^\star$ (see Fig. 9). Finally, it is worth noticing that $\mathcal{L}_\mp$ merge at time $\tau_2^\star$ and then separate again at time $\tau_3^\star$. The motion of these curves is now briefly described.

At the initial time ($\tau = 0$), the curve $\mathcal{L}_+$ collapses to the point $\boldsymbol{w}_2^\star$ (external to $\mathcal{C}$), while $\mathcal{L}_-$ is superimposed to $\mathcal{C}^\star$, which in turn lies inside $\mathcal{C}$. Afterward, $\mathcal{L}_+$ grows and $\mathcal{L}_-$ approaches $\mathcal{C}$, up to touch that circle at the *critical time* $\tau_1^\star$ and to cross it at later ones. In correspondence with the intersection between $\mathcal{L}_-$ and $\mathcal{C}$, the other curve ($\mathcal{L}_+$) becomes non-simple (see Appendix C). The two curves $\mathcal{L}_\mp$ remain separated, until two branch points ($\tilde{z}_{3,4}$) lie inside $\mathcal{C}$. At the *critical time* $\tau_2^\star$, one of them ($\tilde{z}_4$) crosses $\mathcal{C}$ and $\mathcal{L}_\mp$ merge in a new non-simple curve $\mathcal{L}$. The curve $\mathcal{L}$ breaks again in two separated ones at the *critical time* $\tau_3^\star$, when a new branch point ($\tilde{z}_2$) enters in the unit circle. At the successive *critical time* $\tau_4^\star$, $\mathcal{L}_-$ touches $\mathcal{C}$, lying inside $\mathcal{C}$ at later times. At the same time, $\mathcal{L}_+$ becomes simple again. Finally, at the end of the period ($\tau = \pi$), $\mathcal{L}_+$ collapses to the point $\boldsymbol{w}_2^\star$ and $\mathcal{L}_-$ superimposes to the circle $\mathcal{C}^\star$.

The motion of the same curves for the vortices in the second and third rows of Fig. 2 is *qualitatively* different from the one investigated above, but it is not described here for the sake of shortness. However, the main differences are due to the fact that the point $\boldsymbol{w}_2^\star$ and the circle $\mathcal{C}^\star$ are placed in different positions with respect to the unit circle. In particular, $\boldsymbol{w}_2^\star$ lies in both cases inside $\mathcal{C}$ and the circle $\mathcal{C}^\star$ includes $\mathcal{C}$ for the vortex in the second row, while $\mathcal{C}^\star$ is external and it does not include the unit circle for the one in the third row.

About the behaviour of the roots $\boldsymbol{F}_\mp(z;\tau)$ as functions of the point z in a certain neighbourhood of $\mathcal{C}$ and at a fixed time τ, just few key definitions are given here, while a more detailed discussion can be found in Appendix D. As described above, the algebraic structures of these functions contain the square root of a time-dependent quartic polynomial, which has to be calculated by accounting for the motion of its zeros $\tilde{z}_1(\tau)$, $\ldots$, $\tilde{z}_4(\tau)$. A branch of the root is obtained by grouping these points into suitable pairs and joining the points of each of the two pairs through arbitrary cuts, called $\mathcal{T}_+$ and $\mathcal{T}_-$ (due to the fact that, in the early stages of the motion, they are internal to the curves $\mathcal{L}_+$ and $\mathcal{L}_-$, respectively). These cuts must be thought as closed curves having empty insides, their shapes defining the branch of the maps $\boldsymbol{F}_\mp$ under consideration. The limit values of the function $\boldsymbol{F}_+$ [$\boldsymbol{F}_-$] on two superimposed points of $\mathcal{T}_+$ [$\mathcal{T}_-$] from the two sides of the cut are in

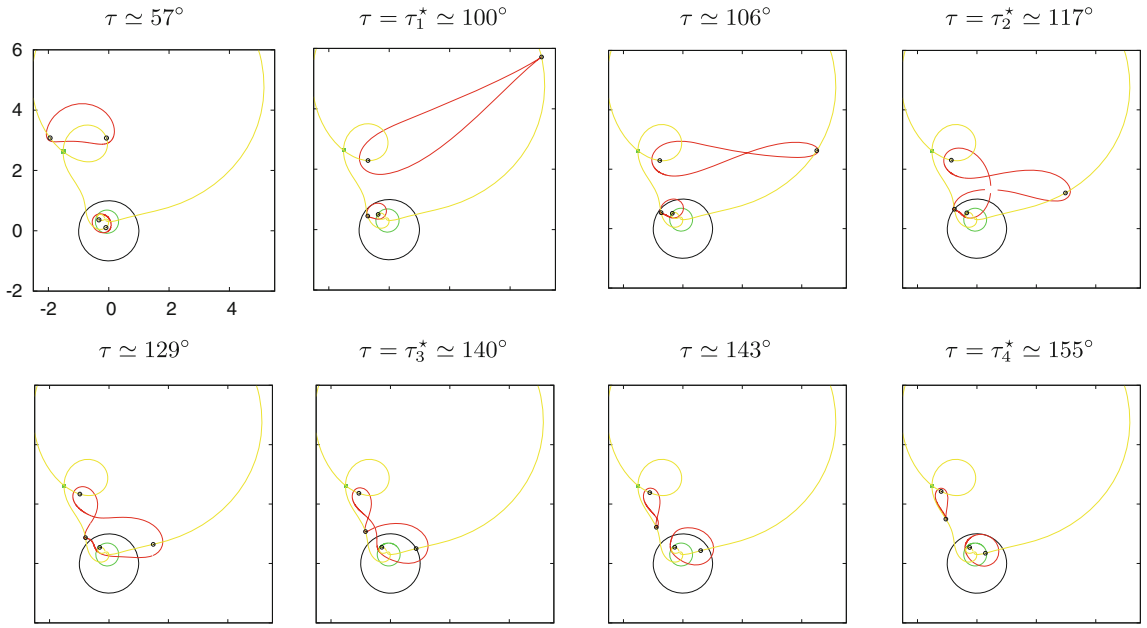

Fig. 3 Curves $\mathcal{L}_\mp$ (*red solid line*) at different times in [0, 180°), for the vortex in the first row of Fig. 2. The point $\boldsymbol{w}_2^\star \equiv \boldsymbol{F}_+(\mathcal{C}; 0)$ and the circle $\mathcal{C}^\star = \boldsymbol{F}_-(\mathcal{C}; 0)$ are drawn (*green*), together with the trajectories (*yellow*) of the branch points (their current positions are indicated with *black circles*). $\mathcal{L}_-$ lies inside $\mathcal{C}$ up to the time $\tau_1^\star$, at which a cusp appears on $\mathcal{L}_+$ (it becomes non-simple up to the time $\tau_4^\star$). Both curves $\mathcal{L}_\mp$ remain separated up to time $\tau_2^\star$, when they merge in a non-simple closed one ($\mathcal{L}$). In turn, $\mathcal{L}$ breaks at time $\tau_3^\star$ in two closed curves $\mathcal{L}_+$ (non-simple and external to $\mathcal{C}$) and $\mathcal{L}_-$ (crossing $\mathcal{C}$). Finally, $\mathcal{L}_-$ returns inside $\mathcal{C}$ at time $\tau_4^\star$, when also $\mathcal{L}_+$ becomes simple again

general different: the function experiences a finite jump in crossing the cut. As a consequence, the image curve $\boldsymbol{F}_+(\mathcal{T}_+)$ [$\boldsymbol{F}_-(\mathcal{T}_-)$] results to be simple and closed. Moreover, it can be shown that it is invariant for the other map $\boldsymbol{F}_-$ [$\boldsymbol{F}_+$]. For this reason, it will be called $\mathcal{I}_-$ [$\mathcal{I}_+$]. Note also that if $\tilde{\boldsymbol{z}}_{1,2}$ are the endpoints of $\mathcal{T}_+$, the transformed points $\tilde{\boldsymbol{Z}}_{1,2} := \boldsymbol{F}_-(\tilde{\boldsymbol{z}}_{1,2}) \in \mathcal{I}_-$ do not depend on the choice of the cut $\mathcal{T}_+$. They are fixed points on the invariant curve $\mathcal{I}_-$. On the basis of the above definitions, the choice of one-to-one branches of the maps $\boldsymbol{F}_\mp$ becomes possible. It is briefly discussed in Appendix D.

6 Results

The above analytical approach is now applied to the study of the motion of non-trivial sample vortices. The initial vortex shapes are chosen among the ones investigated in the paper [11], by giving suitable values to poles and corresponding residues in their Schwarz functions (16). Other results obtained by applying the present approach can be found in [23], even if they are there presented without discussing mathematical details.

In particular, three shapes have been selected (see Fig. 2). The first one has the circle $\mathcal{C}^\star$ inside $\mathcal{C}$ and the point $\boldsymbol{w}_2^\star$ outside, while the second vortex has $\mathcal{C}^\star$ external and including $\mathcal{C}$ and $\boldsymbol{w}_2^\star$ inside the unit circle. Also, the third vortex has $\mathcal{C}^\star$ external to $\mathcal{C}$, but it does not include the unit circle in this case, while $\boldsymbol{w}_2^\star$ still lies inside $\mathcal{C}$. As a consequence, the initial positions of the curves $\mathcal{L}_-$ (superimposed to $\mathcal{C}^\star$) and $\mathcal{L}_+$ (collapsed on the point $\boldsymbol{w}_2^\star$) with respect to $\mathcal{C}$ are different, as well as their dynamics. Different time behaviours of the approximate solutions follow. Furthermore, it is worth remarking that each boundary possesses at the initial time ($\tau = 0$) a structure similar to the initial stage of a filament. It involves a large part of the boundary in the second case, being very small in the first and third ones. However, the first shape is the more interesting one, due to the fact that its initial filament has mean curvature which is opposite to the bulk angular velocity of the vortex. It quickly disappears as the vortex begins to move and a new filament is produced in a different region of the vortex boundary.

Due to the different dynamics of the curves $\mathcal{L}_\mp$, the solutions at 0th and 1st orders approximate in more or less satisfactory ways the numerical ones. In general, the agreement between analytical and numerical solutions is kept until the curve $\mathcal{L}_-$ intersects $\mathcal{C}$. At later times, $\partial P^{(0)}$ becomes non-simple, leading to large errors in the 0th order solution. It will be shown below that the 1st-order solution strongly improves this behaviour.

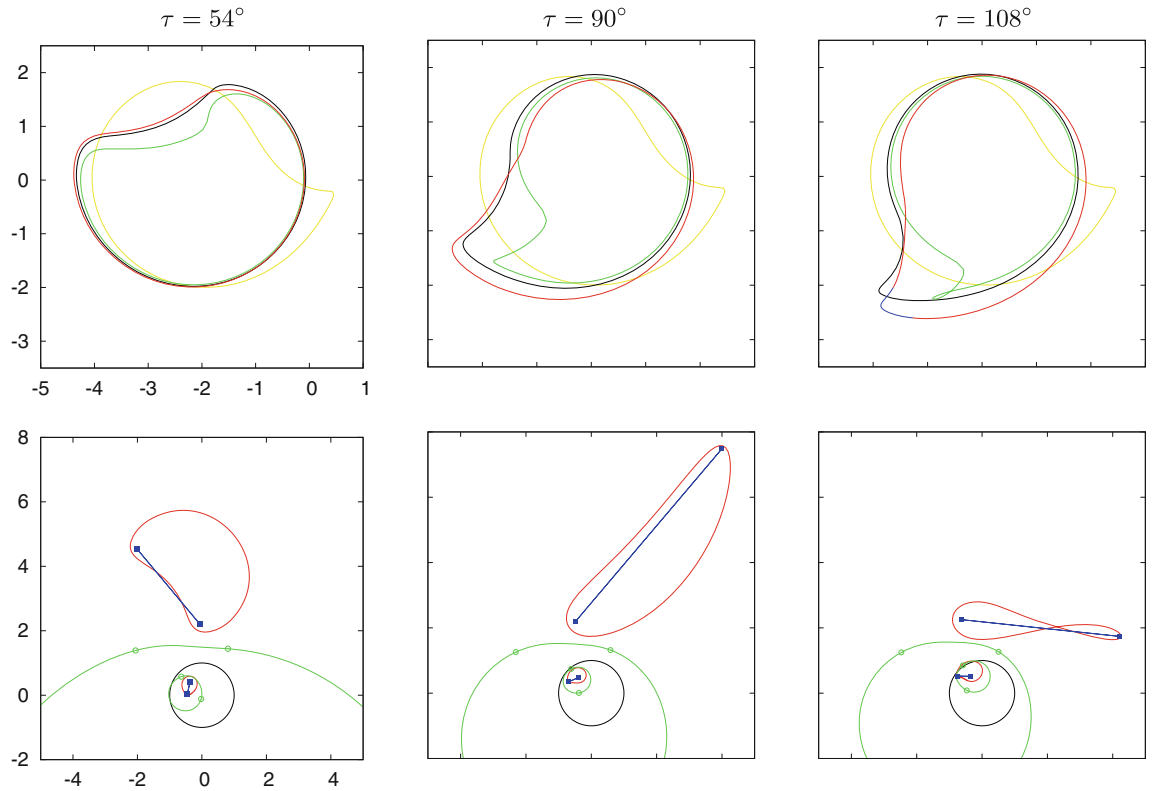

Fig. 4 In the first row, the numerical boundaries (*black lines*) are superimposed to the analytical ones at orders 0 (*green*) and 1 (*red*/*blue*) for the vortex in the first row of Fig. 2. As in this figure, the initial vortex shape is also drawn (*yellow*). In the second row, the curves $\mathcal{L}_\mp$ (*red*), $\mathcal{I}_\mp$ (*green*) as well as the cuts $\mathcal{T}_\mp$ (*blue*) are drawn at the same times. The unit circle is also drawn (*black*), while *symbols* indicate the branch points $\tilde{z}_k$ (*blue*) and the corresponding invariant ones $\tilde{\boldsymbol{Z}}_k$ (*green*) for $k = 1, \ldots, 4$. *Times* are indicated above, in sexagesimal degrees

Roughly speaking, it agrees with the numerical solution up to times of the order of one-fourth of the eddy turnover period.

The analytical solutions for the vortex in the first row of Fig. 2 at orders 0 and 1 are shown in the first row of Fig. 4. The numerical boundaries are also superimposed, together with the initial shape. In the second row, the image curves $\mathcal{L}_\mp$, the invariant ones $\mathcal{I}_\mp$ and the cuts $\mathcal{T}_\mp$ (assumed straight for the sake of simplicity) are drawn at the corresponding times. The picture at time $\tau = 54^\circ$ shows that the disappearance of the original filament and the formation of the new one are accurately captured by the 1st-order solution. On the contrary, the errors of the 0th order solution appear already quite large. The analysis of the corresponding curves $\mathcal{L}_\mp$, $\mathcal{I}_\mp$ and $\mathcal{T}_\mp$ in the second row shows that for a short time, a transition[5] from the configuration in Fig. 11a (Appendix D) to the one in Fig. 11b occurs, the cut $\mathcal{T}_+$ intersecting the curve $\mathcal{L}_+$. During this time, the maps $\boldsymbol{F}_\mp$ behave in a different way, by changing from the functions in the first row of Fig. 12 (Appendix D) to the ones in the second row of the same figure. It follows that two different branches of the function $\boldsymbol{F}_+$ are now needed in order to correctly draw the curve $\mathcal{L}_+$.

The successive motion of the new filament is captured by the approximate solutions in a more qualitative way, as shown by the picture at time $\tau = 90^\circ$ (just before $\tau_1^\star$). At this time, the 0th order solution exhibits a very thin filament with a large loss of circulation, while the 1st-order solution leads to errors in high curvature regions of the vortex core. Note that the cut $\mathcal{T}_+$ does not more intersects $\mathcal{L}_+$, so that the maps $\boldsymbol{F}_\mp$ still behave as in the first row of Fig. 12 (Appendix D).

At the successive time $\tau = 108^\circ$, the 0th order solution breaks down ($\tau_1^\star \simeq 100^\circ$, see the table in Fig. 9), $\partial P^{(0)}$ becoming a non-simple curve. At the same time, in the high curvature regions of vortex core, the errors of the 1st-order solution grow and $\partial P^{(1)}$ rotates somewhat faster than the numerical boundary. However, the 1st-order solution still represents a substantial improvement in the 0th order one. As discussed in Sect. 5, the

[5] This behaviour is due to the present definition of the cuts. In principle, it can be avoided by adopting a curved cut $\mathcal{T}_+$.

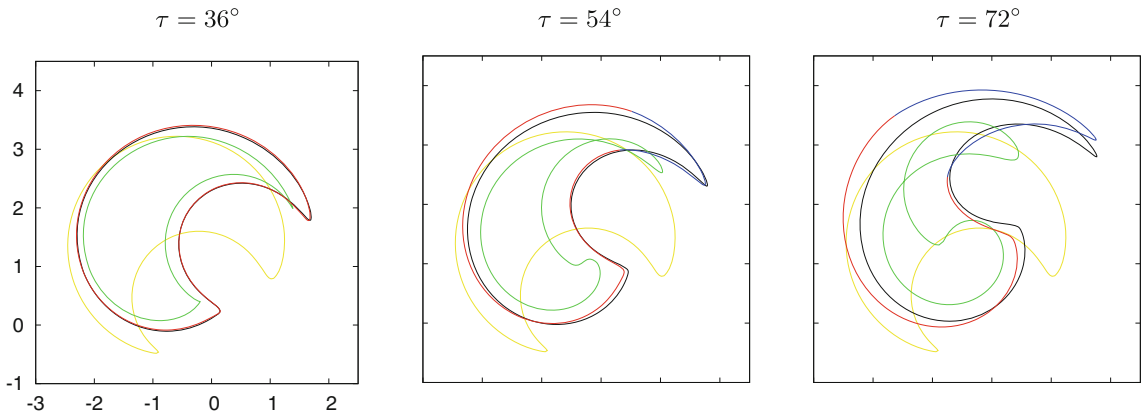

Fig. 5 As in Fig. 4, but for the vortex in the second row of Fig. 2

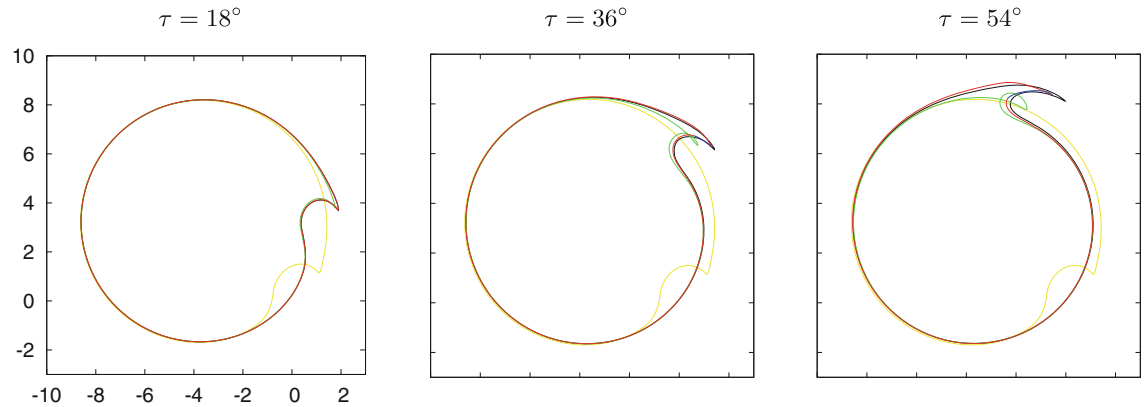

Fig. 6 As in Fig. 4, but for the vortex in the third row of Fig. 2

curve $\mathcal{L}_-$ intersects the unit circle and the curve $\mathcal{L}_+$ (still obtained by using two branches of the function $\boldsymbol{F}_+$) becomes non-simple, intersecting the cut $\mathcal{T}_+$ in two points. The corresponding space behaviour of the maps $\boldsymbol{F}_\mp$ becomes much more complicated. In this condition, the nonlinear term $\boldsymbol{N}$ (14) has to be calculated in a different way with respect to previous times. This fact is accounted for in the first row of Fig. 4 by using two colours for drawing $\partial P^{(1)}$. For $\boldsymbol{\xi}$ running counterclockwise on $\partial P(0)$, it is red (as before) if $\boldsymbol{x}^{(0)}(\boldsymbol{\xi};\tau)$ belongs to the counterclockwise oriented part of $\partial P^{(0)}(\tau)$, while it becomes blue if $\boldsymbol{x}^{(0)}(\boldsymbol{\xi};\tau)$ lies on the clockwise oriented part of the same curve.

Finally, at time $\tau = 126°$, also the 1st-order solution breaks down, the corresponding vortex boundary becoming non-simple.

The analytical approximate solutions for the vortex in the second row of Fig. 2 are drawn in Fig. 5. In this case, the curve $\mathcal{L}_-$ intersects the unit circle in the early stages of the motion ($\tau_1^\star \simeq 38°$, see the table in Fig. 9) and the 0th order boundary becomes quickly non-simple. However, the 1st-order solution strongly improves such behaviour, leading to an excellent agreement with the numerical one in the early stages ($\tau = 36°$, just before $\tau_1^\star$) of the motion. The error with respect to the reference numerical solution slowly grows at later times, as shown by the picture at time $\tau = 54°$. Note that the vortex shape has been experienced a relevant change at this time: the core is rather larger than the initial one as well as the filament appears to be thinner. Finally, the agreement with respect to the reference solution becomes quite poor at later times, as shown by the picture at time $\tau = 72°$.

The dynamics of the vortex in the third row of Fig. 2 is investigated in Fig. 6. This case is the most difficult one, due to the fact that the intersection between $\mathcal{L}_-$ and $\mathcal{C}$ occurs very early ($\tau_1^\star \simeq 23°$, see the table in Fig. 9). As before, the agreement between analytical solutions and reference ones is satisfactory in the first stages of the motion (see the time $\tau = 18°$) and errors grow only after $\tau_1^\star$, when the 0th order solution becomes non-simple. Nevertheless, the 1st-order solution appears to be an excellent approximation at time $\tau = 36°$ and also at time $\tau = 54°$, which is just before the critical time $\tau_2^\star$ (at which $\tilde{z}_4$ goes into the unit circle). This

solution captures easily the motion of the quasi-circular core, but it appears also able to follow the formation of the filament as well as the early stages of its dynamics.

7 Concluding remarks and future work

A nonlinear singular integral equation describing the evolution in time of the Schwarz function of the boundary of a two-dimensional, uniform vortex moving in an isochoric, inviscid fluid has been presented. The nonlinear nature of the equation is due to just one term, involving also the positions on the vortex boundary at the current time. In the author opinion, this equation partially overcomes the relevant difficulties in identifying the changes in the Schwarz function, which occur during the vortex motion. By assuming that the solution of the above equation *exists* and *is unique*, its approximation through a standard technique is also faced. The nonlinear equation is replaced by a hierarchy of linear ones, each of them being forced by the nonlinear term evaluated at the previous order. These linear equations are still singular and their solutions are easily written, leading to new approximate solutions for the time evolution of the Schwarz function of the vortex boundary. In principle, the convergence of the sequence of approximating solutions should be investigated. However, the algebraic complexity of the forcing term grows very rapidly with the order of the approximation; therefore, this analysis appears to be a difficult task at the present time. It is here replaced by the experimental comparison with the numerical simulations of the vortex motion.

Solutions at the 0th and 1st orders are given. They are also applied to a class of vortices, the kinematics of which is analytically known. The 0th order solution agrees with the numerical one for very small times, the corresponding vortex shape becoming quickly non-simple. The 1st-order solution strongly improves this behaviour. Its agreement with the numerical one appears to be very satisfactory for times of the order of one-fourth of the eddy turnover period, becoming more and more qualitative at later times. However, the 1st-order solution is able to follow larger changes in the vortex shape. To the best of the author's knowledge, there is not another analytical approach which behaves in the same way.

Behind the present solutions, a lot of interesting mathematical devices have been found. They are not specific for the particular vortex shapes here investigated. First of all, on the periodic changes (having period $T = 4\pi/\omega$) of the 0th order solution $\boldsymbol{S}^{(0)}$ (12), a non-periodic time evolution is superimposed, due to the presence of convolutions in time inside the 1st-order solution (15). As shown by the form (14) of the nonlinear term $\boldsymbol{N}$, the non-periodic time evolution is driven by the periodic motion of the curves on which the displacement ratio $\boldsymbol{h}^{(0)}$ vanishes. Moreover, two different algebraic structures of the 1st-order solution have been found. The passage from one to the other is induced by a change in the nonlinear term $\boldsymbol{N}$ occurring at the time in which the 0th order vortex boundary becomes non-simple ($\tau_1^\star$). Finally, as it happens to the 0th order solution, the physical meaning of the 1st order one is lost at the time in which $\partial P^{(1)}$ becomes a non-simple curve.

What do we learn from the above solutions for the fluid dynamics?

A first important contribution concerns the filamentation of the vortex boundary. Its appearance is related to the fact that $\partial P^{(0)}$ becomes at a certain time a non-simple curve. As shown in Sect. 6, in this condition, the 1st-order solution (15) corrects the above unphysical behaviour of the 0th order one, so that a neighbourhood of the double point on $\partial P^{(0)}$ becomes a thin layer in $\partial P^{(1)}$, that is, a filament. As a consequence, the appearance as well as the *time* (τ) and the *Lagrangian position* ($\boldsymbol{\xi}$) in which the filamentation occurs can be predicted, by searching for the double point of the function $\boldsymbol{x}^{(0)}(\boldsymbol{\xi};\tau)$. Note also that despite the filamentation can be predicted by means of the linear solution (13), its description becomes possible if and only if nonlinear effects are accounted for.

Another aspect of the self-induced dynamics that has been explained concerns the effects of the nonlinearity (in particular, at the first order) on the motion of the vortex core. As a matter of fact, if the core is nearly circular (as in the case of Fig. 6), the linear approximation (13) works very well (see also the discussion for the elliptical vortex in Sect. 3). Perhaps, this behaviour could be related to the success in using series representations of the solution in that case. On the other hand, when the core experiences large deformations (as in the case of Fig. 4), or it grows due to an axisymmetrization process (like in Fig. 5), the linear approximation becomes poor. The nonlinear term appears to be essential in order to properly follow the motion of these vortex cores.

Several issues still remain to be investigated. Firstly, it is important to analyse the initial stages of the dynamics of the (Eulerian) Schwarz function $\boldsymbol{\Phi}$. This can be done by building the inverse of the relation (13), so that the Lagrangian position $\boldsymbol{\xi} \in \partial P(0)$ is rewritten at a time τ as a function of the Eulerian one $\boldsymbol{x} \in \partial P^{(0)}(\tau)$. An approximation of the (Eulerian) Schwarz function on the current boundary follows from Eq. (12) by assuming: $\boldsymbol{\Phi}(\boldsymbol{x};\tau) \simeq \boldsymbol{S}^{(0)}[\boldsymbol{\xi}(\boldsymbol{x};\tau);\tau]$. Its analytic continuation outside that boundary could give

important information about the initial stages of the dynamics of $\boldsymbol{\Phi}$. In principle, the same can also be made with the 1st-order solution, at least locally (i.e. in a neighbourhood of some special point of the vortex boundary), even if huge algebraic difficulties must be overcome. The analysis of the spatial behaviour of the roots $\boldsymbol{F}_{\mp}$ outlined in Sect. 5 (and in Appendix D) represents a first important step along this way.

The present 1st-order solution can also be improved. As a matter of fact, the integral on $\partial P(0)$ in the 1st-order Schwarz function $\boldsymbol{S}^{(1)}$ (15) is computed in a numerical way at the present time, despite it could be written in terms of several elliptic ones by means of a lot of algebraic work.

Finally, it will be important to understand if the *algebraic structure* of the Lagrangian Schwarz function changes abruptly once the motion starts, or if it is retained, at least for small times (as in the author opinion). This issue is under investigation at the present time. It is approached by enforcing the conservation of the structure of $\boldsymbol{S}$ in its evolution Eq. (3), which leads to a system of nonlinear ordinary differential equations describing the time evolution of the poles ($z_{1,2}$) and of the residues ($\boldsymbol{a}_{1,2}$) in the form (16) of the Schwarz function. Also in this case, its physical meaning will be checked by means of experimental comparisons with contour dynamics simulations of the vortex motion.

Acknowledgements The author would like to thank the anonymous Referees, whose suggestions greatly improved the paper.

Appendix A : Laplace antitransform of $\tilde{\boldsymbol{F}}(y)/(y+ia)$

If $\tilde{\boldsymbol{F}}(y) := \mathcal{L}[\boldsymbol{F}](y)$ is the Laplace transform of $\boldsymbol{F}(x)$ and a is an arbitrary real number, the following relation:

$$\frac{\mathrm{d}}{\mathrm{d}x}\left\{\mathrm{e}^{\boldsymbol{i}ax}\mathcal{L}^{-1}\left[\frac{\tilde{\boldsymbol{F}}(y)}{y+\boldsymbol{i}a}\right](x)\right\} = \mathrm{e}^{\boldsymbol{i}ax}\boldsymbol{F}(x)$$

is valid. By integrating in x, it becomes

$$\mathcal{L}^{-1}\left[\frac{\tilde{\boldsymbol{F}}(y)}{y+\boldsymbol{i}a}\right](x) = \mathrm{e}^{-\boldsymbol{i}ax}\left\{\int_0^x \mathrm{d}\xi\,\boldsymbol{F}(\xi)\mathrm{e}^{\boldsymbol{i}a\xi} + \mathcal{L}^{-1}\left[\frac{\tilde{\boldsymbol{F}}(y)}{y+\boldsymbol{i}a}\right](0)\right\}. \tag{22}$$

The second term in the right-hand side of Eq. (22) vanishes. Indeed, by exchanging the singular and the regular integrals that term becomes (μ is a real number greater than the abscissa of convergence of $\tilde{\boldsymbol{F}}$):

$$\begin{aligned}\mathcal{L}^{-1}\left[\frac{\tilde{\boldsymbol{F}}(y)}{y+\boldsymbol{i}a}\right](0) &= \frac{1}{2\pi\boldsymbol{i}}\int_{\mu-\boldsymbol{i}\infty}^{\mu+\boldsymbol{i}\infty}\mathrm{d}y\,\frac{\tilde{\boldsymbol{F}}(y)}{y+\boldsymbol{i}a}\\ &= \int_0^{+\infty}\mathrm{d}\xi\,\boldsymbol{F}(\xi)\frac{1}{2\pi\boldsymbol{i}}\int_{\mu-\boldsymbol{i}\infty}^{\mu+\boldsymbol{i}\infty}\mathrm{d}y\,\frac{\mathrm{e}^{-y\xi}}{y+\boldsymbol{i}a},\end{aligned}$$

in which the inner integral is zero. This fact can be proved by integrating (via the residue theorem) the function $\mathrm{e}^{-y\xi}/(y+\boldsymbol{i}a)$ on the rectangle in Fig. 7 and evaluating the limit as $M \to +\infty$:

$$\frac{1}{2\pi\boldsymbol{i}}\int_{\mu-\boldsymbol{i}\infty}^{\mu+\boldsymbol{i}\infty}\mathrm{d}y\,\frac{\mathrm{e}^{-y\xi}}{y+\boldsymbol{i}a} + \frac{1}{2\pi\boldsymbol{i}}\int_{-\mu+\boldsymbol{i}\infty}^{-\mu-\boldsymbol{i}\infty}\mathrm{d}y\,\frac{\mathrm{e}^{-y\xi}}{y+\boldsymbol{i}a} = \mathrm{e}^{\boldsymbol{i}a\xi}.$$

By performing the change of variable from y to $y' = -y$ in the second integral, it gives $\mathrm{e}^{\boldsymbol{i}a\xi}$, so that the first integral in the above equation results to be zero. Equation (22) becomes

$$\mathcal{L}^{-1}\left[\frac{\tilde{\boldsymbol{F}}(y)}{y+\boldsymbol{i}a}\right](x) = \mathrm{e}^{-\boldsymbol{i}ax}\int_0^x \mathrm{d}\xi\,\boldsymbol{F}(\xi)\mathrm{e}^{\boldsymbol{i}a\xi}. \tag{23}$$

Note that the well known rule about the Laplace transform of the integral of $\boldsymbol{F}$ can be also obtained, by enforcing $a = 0$ in Eq. (23).

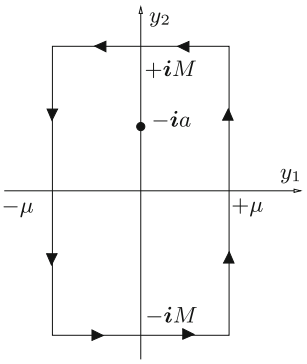

Fig. 7 Integration path

Appendix B : Branch points of the maps $\boldsymbol{F}_{\mp}$

In the present appendix, the motion of the four branch points $\tilde{z}_1, \ldots, \tilde{z}_4$ of the functions $\boldsymbol{F}_{\mp}$ is investigated.

They are not calculated by their definition (i.e. as roots of the discriminant of $\boldsymbol{P}$), being also roots of a simpler quartic. Indeed, the quadratic equation $\boldsymbol{P}(\tilde{z}_k, \boldsymbol{\tau} \mid \boldsymbol{\zeta}) = 0$ ($k = 1, \ldots, 4$) possesses two superimposed roots, say $\tilde{\boldsymbol{\zeta}}_k$ (called kth *image* branch point), due to the fact that its discriminant vanishes. As a consequence, the reciprocity (21) implies that $\tilde{\boldsymbol{\zeta}}_k$ satisfies also the quartic equation $\boldsymbol{P}(\boldsymbol{\zeta}, \tau \mid \boldsymbol{\zeta}) = 0$. Once a root $\tilde{\boldsymbol{\zeta}}_k$ of that equation has been calculated, the corresponding branch point $\tilde{z}_k$ follows, by using the symmetry of $\boldsymbol{P}$.

In Fig. 8, the motion of the image branch points $\tilde{\boldsymbol{\zeta}}_1, \ldots, \tilde{\boldsymbol{\zeta}}_4$ (column a) and of the branch points $\tilde{z}_1, \ldots, \tilde{z}_4$ (b and c) during a period are shown for the vortices in the three rows of Fig. 2. The image point $\tilde{\boldsymbol{\zeta}}_1$ starts from z_{io}^- (green symbol) in the column a and runs on the red curve, until it reaches z_{io}^+ (blue). The corresponding branch point $\tilde{z}_1$ moves on the red curve in the column b, by starting and ending on the point $\boldsymbol{w}_2^\star$ (turquoise). The image point $\tilde{\boldsymbol{\zeta}}_2$ starts from z_{io}^+ (blue) and moves on the black curve (column a), until it reaches $\boldsymbol{w}_2^\star$. In correspondence with such a motion, the branch point $\tilde{z}_2$ runs on the large black curve (column b). It starts from $\boldsymbol{w}_2^\star$, crosses $\mathcal{C}$ (green line) at time $\tau_3^\star$ and reaches the point $\boldsymbol{w}_2^{\star\star} = \boldsymbol{\zeta}^\star(\boldsymbol{w}_2^\star)$ (green). The image point $\tilde{\boldsymbol{\zeta}}_3$ runs on a closed trajectory (red), by starting and ending at $\boldsymbol{w}_2^\star$. Also, the corresponding branch point $\tilde{z}_3$ moves on a closed curve (red), which starts and ends in $\boldsymbol{w}_2^{\star\star}$. The image point $\tilde{\boldsymbol{\zeta}}_4$ starts from $\boldsymbol{w}_2^\star$ and runs on the black curve, until it reaches the point z_{io}^-. In correspondence, the branch point $\tilde{z}_4$ moves on the black curve starting from $\boldsymbol{w}_2^{\star\star}$. It crosses $\mathcal{C}$ at time $\tau_2^\star$ and then reaches the point $\boldsymbol{w}_2^\star$. Note that the trajectories of $\tilde{z}_2$ and $\tilde{z}_4$ intersect, but these points reach the intersection at different times.

Appendix C : Critical times evaluation

In the present appendix, the calculations of several quantities related to the motion of the curves $\mathcal{L}_{\mp}$ (see Sect. 5) are summarized.

As discussed in Sect. 3, the algebraic structure of the nonlinear term (14) depends on the topology of $\partial P^{(0)}$, which becomes non-simple at times $\tau_1^\star < \tau < \tau_4^\star$. At these times, the points $z_{\mp}^\star = \exp(\mathrm{i}\theta_{\mp}^\star)$ in which $\mathcal{L}_-$ intersects $\mathcal{C}$ are then needed for evaluating $\boldsymbol{N}$. The corresponding angles $\theta_{\mp}^\star$ are drawn versus time in Fig. 9 for the three vortices in Fig. 2. They are calculated in the following way.

As it occurs for any point on $\mathcal{L}_-$, also the intersection $z_-^\star$ comes from a certain point $z \in \mathcal{C}$ through the map $\boldsymbol{F}_-$: $z_-^\star = \boldsymbol{F}_-(z)$ (hereafter, times will be omitted for the sake of shortness), see Fig. 10a. The other root of $\boldsymbol{P}$, that is, $\boldsymbol{F}_+(z) =: \boldsymbol{\chi}$, lies outside $\mathcal{C}$. Examine now what happens if the coefficients of $\boldsymbol{P}$ are evaluated in $z_-^\star$, instead of z. Due to the symmetry of $\boldsymbol{P}$, $\boldsymbol{P}(z_-^\star \mid z) = 0$ so that $\boldsymbol{F}_-(z_-^\star) = z$ ($\boldsymbol{F}_+(z_-^\star)$ cannot lie on $\mathcal{C}$), that is, z is just the other intersection (called $z_+^\star$) between $\mathcal{L}_-$ and $\mathcal{C}$. From the reciprocity (21): $\boldsymbol{P}[\boldsymbol{F}_-(z_+^\star) \mid \boldsymbol{F}_+(z_+^\star)] = \boldsymbol{P}(z_-^\star \mid \boldsymbol{\chi}) = 0$: $\boldsymbol{F}_+(z_-^\star)$ still gives $\boldsymbol{\chi}$, see Fig. 10b. In this way, the intersection points $\{z_+^\star, z_-^\star\}$ between $\mathcal{L}_-$ and $\mathcal{C}$ are characterized by the fact that each point is a root of $\boldsymbol{P}$, the coefficients of which being evaluated on the other point, that is, $\boldsymbol{F}_-(z_+^\star) = z_-^\star$ and $\boldsymbol{F}_-(z_-^\star) = z_+^\star$. The other root lies always in $\boldsymbol{\chi}$ ($\boldsymbol{F}_+(z_+^\star) = \boldsymbol{F}_+(z_-^\star) = \boldsymbol{\chi}$). As a consequence, $\mathcal{L}_+$ intersects itself in correspondence with the point $\boldsymbol{\chi}$ and then it is a non-simple curve. Furthermore, due to the symmetry of $\boldsymbol{P}$, the roots of the polynomial evaluated in $\boldsymbol{\chi}$ are just $z_-^\star$ and $z_+^\star$, so that $\boldsymbol{\chi}$ can be calculated by enforcing that both roots (in $\boldsymbol{\zeta}$) of the

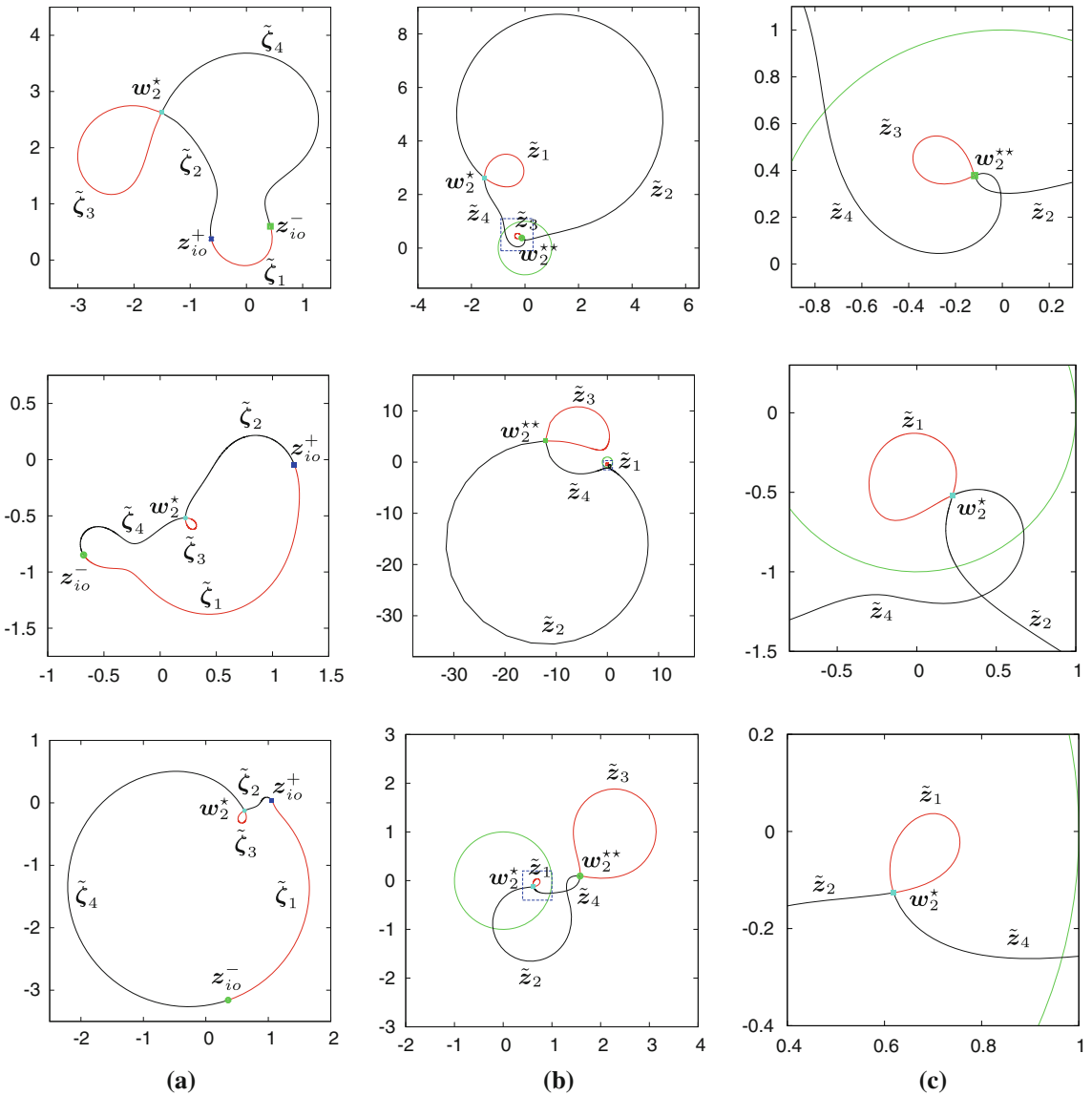

Fig. 8 For the vortices in Fig. 2, the trajectories of $\tilde{\boldsymbol{\zeta}}_{1,\dots,4}$ (column **a**) and of $\tilde{\boldsymbol{z}}_{1,\dots,4}$ (column **b**) are drawn during a period. Finally, in (**c**), there are enlargements of the squares (*blue dashed lines*) in (**b**)

polynomial $\boldsymbol{P}(\boldsymbol{\chi} \mid \boldsymbol{\zeta})$ lie on $\mathcal{C}$ (see Fig. 10c). An easy way to perform this calculation consists in rewriting the point $\boldsymbol{\zeta} \in \mathcal{C}$ as $(1 + \boldsymbol{i}\eta)/(1 - \boldsymbol{i}\eta)$, η being a (unknown) real number. Hence, the equation $\boldsymbol{P}(\boldsymbol{\chi} \mid \boldsymbol{\zeta}) = 0$ becomes: $\boldsymbol{v}_0\eta^2 + 2\boldsymbol{v}_1\eta + \boldsymbol{v}_2 = 0$, the coefficients being quadratic polynomials in $\boldsymbol{\chi}$. Due to the fact that the above equation has *two real roots* ($\eta_\mp$), its coefficients (viewed as vectors in the plane) must be parallel. As a consequence, two real numbers t and s exist, such that $\boldsymbol{v}_1 = t\boldsymbol{v}_0$ and $\boldsymbol{v}_2 = s\boldsymbol{v}_0$. Once they are known, the roots are $\eta_\mp = -t \mp \sqrt{t^2 - s}$.

The numbers t and s are determined by rereading the above two conditions on the coefficients $\boldsymbol{v}_0$, $\boldsymbol{v}_1$ and $\boldsymbol{v}_2$ as a linear system in $\boldsymbol{\chi}$ and $\boldsymbol{\chi}^2$, so that

$$\boldsymbol{\chi} = \frac{\boldsymbol{m}_{12} + \boldsymbol{m}_{22}t + \boldsymbol{m}_{32}s}{\boldsymbol{m}_{13} + \boldsymbol{m}_{23}t + \boldsymbol{m}_{33}s}, \quad \boldsymbol{\chi}^2 = \frac{\boldsymbol{m}_{11} + \boldsymbol{m}_{21}t + \boldsymbol{m}_{31}s}{\boldsymbol{m}_{13} + \boldsymbol{m}_{23}t + \boldsymbol{m}_{33}s}, \tag{24}$$

the quantity $\boldsymbol{m}_{kh}$ $(k, h = 1, 2, 3)$ depending on time, only. However, solutions (24) can be accepted if and only if

$$\left(\frac{\boldsymbol{m}_{12} + \boldsymbol{m}_{22}t + \boldsymbol{m}_{32}s}{\boldsymbol{m}_{13} + \boldsymbol{m}_{23}t + \boldsymbol{m}_{33}s}\right)^2 = \frac{\boldsymbol{m}_{11} + \boldsymbol{m}_{21}t + \boldsymbol{m}_{31}s}{\boldsymbol{m}_{13} + \boldsymbol{m}_{23}t + \boldsymbol{m}_{33}s}.$$

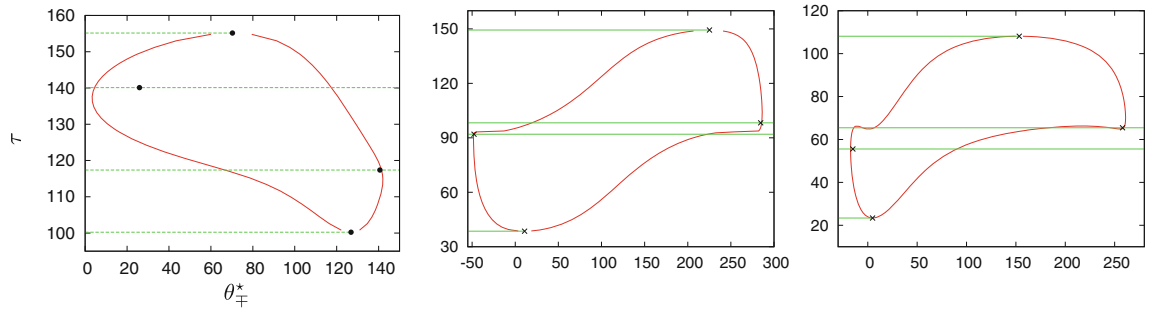

	time	*angle*	*time*	*angle*	*time*	*angle*
$\tau_1^\star$	$100^\circ\ 13'\ 31''$	$126^\circ\ 50'\ 29''$	$38^\circ\ 33'\ 22''$	$10^\circ\ 50'\ 5''$	$23^\circ\ 23'\ 34''$	$4^\circ\ 54'\ 58''$
$\tau_2^\star$	$117^\circ\ 22'\ 53''$	$140^\circ\ 37'\ 40''$	$91^\circ\ 59'\ 29''$	$-47^\circ\ 49'\ 10''$	$55^\circ\ 33'\ 31''$	$-15^\circ\ 2'\ 28''$
$\tau_3^\star$	$140^\circ\ 6'\ 20''$	$25^\circ\ 55'\ 24''$	$98^\circ\ 15'\ 10''$	$284^\circ\ 35'\ 1''$	$65^\circ\ 26'\ 6''$	$257^\circ\ 58'\ 35''$
$\tau_4^\star$	$155^\circ\ 9'\ 3''$	$70^\circ\ 15'\ 56''$	$149^\circ\ 21'\ 38''$	$225^\circ\ 11'\ 44''$	$108^\circ\ 7'\ 29''$	$153^\circ\ 24'\ 47''$

Fig. 9 Angles $\theta_\mp^\star$ (sexagesimal degrees) versus τ (sexagesimal degrees) for the sample vortices of Fig. 2 (from the left to the right). Critical times and angles are also indicated with *green lines* and *black symbols*, respectively. Their *numerical values* (in sexagesimal degrees) are given in the table

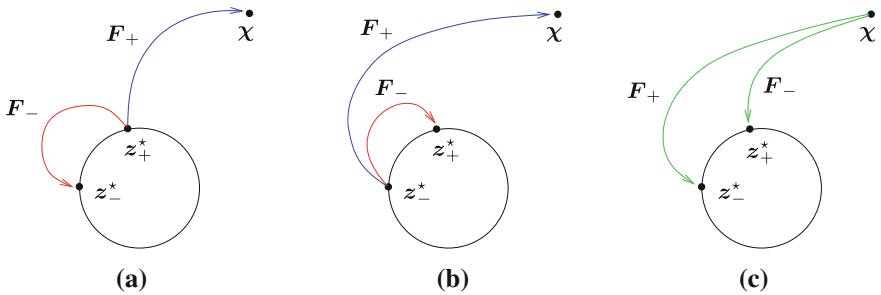

Fig. 10 At a time $\tau_1^\star < \tau < \tau_4^\star$, assume that $\boldsymbol{P}(z_+^\star;\boldsymbol{\tau}\mid\boldsymbol{\zeta})$ has one root on $\mathcal{C}$, named as $z_-^\star := \boldsymbol{F}_-(z_+^\star;\tau)$ (*red line*, **a**) and another one in $\boldsymbol{\chi} := \boldsymbol{F}_+(z_+^\star;\tau)$ (*blue*, **a**), outside $\mathcal{C}$. Hence, the polynomials evaluated in $z_-^\star$ (*red*, **b**) and in $\boldsymbol{\chi}$ (*green*, **c**) have one of their two roots in $z_+^\star$. Moreover, $\boldsymbol{\chi}$ is root of the polynomial evaluated in $z_-^\star$ (*blue*, **b**), as well as $z_-^\star$ is root of the polynomial evaluated in $\boldsymbol{\chi}$ (*green*, **c**)

In real terms, the above relation assumes the geometrical meaning of intersection between two conics in the plane (t,s), leading to the definition of the numbers t and s such that $s \le t^2$. The point $\boldsymbol{\chi}$ follows by the formula (24), as well as the numbers $\eta_\mp$ and the corresponding intersections $z_\mp^\star = (1+\boldsymbol{i}\eta_\mp)/(1-\boldsymbol{i}\eta_\mp) \in \mathcal{C}$.

The calculation of the critical times $\tau_{1,4}^\star$ is performed by enforcing that $s = t^2$ $(\eta_- = \eta_+)$ and viewing the above intersection between two conics as a system of quartic equations in t:

$$\begin{cases} c_0' t^4 + c_1' t^3 + c_2' t^2 + c_3' t + c_4' = 0, \\ c_0'' t^4 + c_1'' t^3 + c_2'' t^2 + c_3'' t + c_4'' = 0. \end{cases}$$

the coefficients of which depend on the time τ and then are unknown. In order to calculate t and the time, a "*reduction*" technique is employed, as summarized below. The above system is solved with respect to t^3 and t^4, and this solution is handled to eliminate $t^4 = t^3 \cdot t$, thus obtaining the new system of two cubics:

$$\begin{cases} d_0' t^3 + d_1' t^2 + d_2' t + d_3' = 0, \\ d_0'' t^3 + d_1'' t^2 + d_2'' t + d_3'' = 0. \end{cases}$$

Again, the above system is solved with respect to t^2 and t^3, and t^3 is eliminated:

$$\begin{cases} e_0' t^2 + e_1' t + e_2' = 0, \\ e_0'' t^2 + e_1'' t + e_2'' = 0. \end{cases}$$

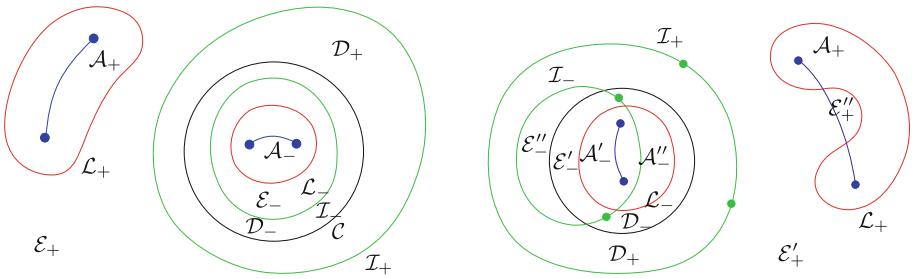

Fig. 11 Sketches of the curves in the first and late stages of the motion, in the absence (**a**) and in the presence (**b**) of intersections between $\mathcal{I}_-$ and $\mathcal{L}_-, \mathcal{C}$ (or $\mathcal{T}_+$ and $\mathcal{L}_+$)

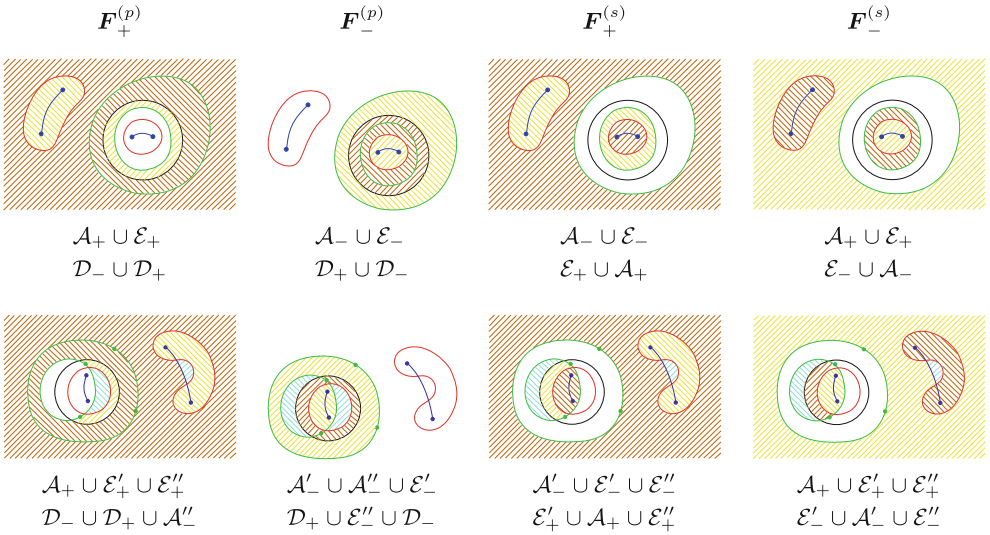

Fig. 12 Principal and secondary maps in the absence (first row) and in the presence of intersections (second) between $\mathcal{I}_-$ and $\mathcal{L}_-, \mathcal{C}$. Each region in the domain is mapped onto the subset of the range having the same colour. Domains (first row) and ranges (second) are listed below each figure. Regions belonging at the same time to the domains and to the ranges of the principal branches are listed only one time (in the domain, or in the range), for the sake of shortness

Finally, the system is solved in t and t^2, leading to the following definition of t and to the compatibility constraint:

$$t = \frac{e'_2 e''_0 - e''_2 e'_0}{e'_0 e''_1 - e''_0 e'_1} \quad \text{provided that:} \quad (e'_1 e''_2 - e''_1 e'_2)(e'_0 e''_1 - e''_0 e'_1) = (e'_2 e''_0 - e''_2 e'_0)^2. \tag{25}$$

The constraint (25) is reread as an algebraic equation in time, which is solved through a Newton method. The times $\tau^\star_{1,4}$ follow, as well as the points in which $\mathcal{L}_-$ touches $\mathcal{C}$.

Finally, the calculation of the critical times $\tau^\star_{2,3}$ is performed by enforcing that the discriminant of the polynomial $\boldsymbol{P}(z; \boldsymbol{\tau} \mid \boldsymbol{\zeta})$ (20) vanishes on a point $z = (1 + i\eta)/(1 - i\eta) \in \mathcal{C}$. In this way, a complex quartic equation in η is obtained. It is viewed as a system of two real ones, which is solved through the above "*reduction*" technique.

Appendix D : Behaviour of $\boldsymbol{F}_\mp$ as functions of z

In this appendix, several details about the behaviour of the maps $\boldsymbol{F}_\mp$ as functions of z are given. The present analysis is different from classical ones (e.g. see [24,25]) which are usually aimed at building a unique monodrome function on a two-sheeted Riemann surface by means of both the above roots. Instead, they are here

investigated as two different functions of z and their one-to-one branches are identified. Time dependences will be omitted for the sake of shortness.

In order to select one-to-one branches of the map $\boldsymbol{F}_+$ [$\boldsymbol{F}_-$], the following definitions are introduced. The action of the map $\boldsymbol{F}_+$ [$\boldsymbol{F}_-$] on the complex plane is split in a *principal branch* (indicated with the superscript "$^{(p)}$"), defined on the domain bounded by the curves $\mathcal{T}_+$ [$\mathcal{T}_-$] and $\mathcal{I}_- = \boldsymbol{F}_+(\mathcal{T}_+)$ [$\mathcal{I}_+ = \boldsymbol{F}_-(\mathcal{T}_-)$], and a *secondary* one ("$^{(s)}$") defined on the complementary domain, bounded by the curves $\mathcal{I}_-$ [$\mathcal{I}_+$] and $\mathcal{T}_-$ [$\mathcal{T}_+$]. On $\mathcal{I}_-$ [$\mathcal{I}_+$], principal and secondary branches assume the same values. The range of $\boldsymbol{F}_+^{(p)}$ [$\boldsymbol{F}_-^{(p)}$] coincides with its domain, while the range of $\boldsymbol{F}_+^{(s)}$ [$\boldsymbol{F}_-^{(s)}$] is the region bounded by the curves $\mathcal{T}_+$ [$\mathcal{T}_-$] and $\mathcal{I}_+$ [$\mathcal{I}_-$]. Note that: *I*) the unit circle, or a subset of it, lies always inside the domains of the principal branches; *II*) the domain of $\boldsymbol{F}_+^{(s)}$ is the range of $\boldsymbol{F}_-^{(s)}$ and vice versa.

By using the symmetry of $\boldsymbol{P}$, it can be shown that the principal branches are self-inverse, that is, if $\boldsymbol{I}$ is the identity, the following relations hold as follows: $\boldsymbol{F}_+^{(p)} \circ \boldsymbol{F}_+^{(p)} = \boldsymbol{I}$ and $\boldsymbol{F}_-^{(p)} \circ \boldsymbol{F}_-^{(p)} = \boldsymbol{I}$. At the same time, the secondary branches result to be one the inverse of the other, that is, $\boldsymbol{F}_-^{(s)} \circ \boldsymbol{F}_+^{(s)} = \boldsymbol{I}$ and $\boldsymbol{F}_+^{(s)} \circ \boldsymbol{F}_-^{(s)} = \boldsymbol{I}$. They can be also represented as compositions of the principal branches. Indeed, by using the reciprocity (21), the relations $\boldsymbol{F}_+^{(s)} = \boldsymbol{F}_+^{(p)} \circ \boldsymbol{F}_-^{(p)}$ and $\boldsymbol{F}_-^{(s)} = \boldsymbol{F}_-^{(p)} \circ \boldsymbol{F}_+^{(p)}$ are found.

The above positions, as well as their consequences, lead to a complete definition of the spatial behaviour of the maps $\boldsymbol{F}_\mp$. As a sample case, consider the vortex at the first row of Fig. 2. Figure 3 shows that at times $0 < \tau < \tau_1^\star$, or $\tau_4^\star < \tau < \pi$, $\mathcal{L}_-$ does not intersect $\mathcal{C}$. Moreover, two branch points lie inside $\mathcal{C}$ and two outside. In Fig. 11, the unit circle (black line), its images through the maps $\boldsymbol{F}_\mp$ ($\mathcal{L}_\mp$, red), the branch cuts ($\mathcal{T}_\mp$, blue) and their images through the maps $\boldsymbol{F}_\mp$ ($\mathcal{I}_\mp$, green) are sketched in the absence (*a*) and in the presence (*b*) of intersections between $\mathcal{I}_-$ and $\mathcal{L}_-$ (or $\mathcal{C}$). The names used for the different regions of the complex plane are also indicated. For example, the regions between $\mathcal{T}_\mp$ and $\mathcal{L}_\mp$ are named as $\mathcal{A}_\mp$, between $\mathcal{L}_\mp$ and $\mathcal{I}_\mp$ as $\mathcal{E}_\mp$ and the regions between $\mathcal{I}_\mp$ and $\mathcal{C}$ as $\mathcal{D}_\mp$. Unless the cuts are defined in an *ad hoc* way, $\mathcal{T}_+$ intersects $\mathcal{L}_+$ during the initial stage of the motion, so that the region $\mathcal{E}_+$ between $\mathcal{I}_+$ and $\mathcal{L}_+$ divides in the subsets $\mathcal{E}'_+$ and $\mathcal{E}''_+$, this latter just trapped between the cut and $\mathcal{L}_+$. Another important consequence is that $\mathcal{I}_-$ cuts $\mathcal{L}_-$, so that $\mathcal{A}_-$ is in turn divided in two subsets, internal ($\mathcal{A}'_-$) and external ($\mathcal{A}''_-$) to $\mathcal{I}_-$. This curve intersects also $\mathcal{C}$, so that the region $\mathcal{E}_-$ inside $\mathcal{I}_-$, but outside $\mathcal{L}_-$, results to be divided in the subsets $\mathcal{E}'_-$ (internal to the unit circle) and $\mathcal{E}''_-$.

From the above analysis, the action of the maps $\boldsymbol{F}_\mp$ on the complex plane sketched in Fig. 12 is easily deduced. In this figure, any subset of the domain is mapped onto the subset of the range having the same colour. Furthermore, the action of the secondary branches (third and fourth pictures from the left) follows from the above rules in terms of the principal ones.

By following these lines, the present analysis can be extended to any time, without substantial difficulties. However, this extension is not discussed here for the sake of shortness.

References

1. Aref, H. (ed.): IUTAM Symposium on 150 Years of Vortex Dynamics. IUTAM Bookseries, Vol. 20. In: Proceedings of the IUTAM Symposium "150 Years of Vortex Dynamics" held at the Technical University of Denmark, October 12–16, 2008. Springer, Heidelberg (2010)
2. Chemin, J.Y.: Persistance de structures géométriques dans les fluides incompressibles bidimensionnels. Annales Scientifiques E. N. S. **26-4**, 1–16 (1993)
3. Bertozzi, A.L., Constantin, P.: Global regularity for vortex patches. Commun. Math. Phys. **152-1**, 19–28 (1993)
4. Majda, A.J., Bertozzi, A.L.: Vorticity and Incompressible Flow. Cambridge University Press, Cambridge (2002)
5. Buttke, T.F.: The observation of singularities in the boundary of patches of constant vorticity. Phys. Fluids A **1**, 1283–1285 (1989)
6. Dritschel, D.G., McIntyre, M.E.: Does contour dynamics go singular? Phys. Fluids A **2**, 748–753 (1990)
7. Saffman, P.G.: Vortex Dynamics. Cambridge University Press, Cambridge (1992)
8. Zabusky, N.J., Hughes, M.H., Roberts, K.V.: Contour dynamics for the Euler equations in two dimensions. J. Comput. Phys. **48**, 96–106 (1979)
9. Dritschel, D.G.: Contour dynamics and contour surgery: numerical algorithms for extended high-resolution modeling of vortex dynamics in two-dimensional, inviscid, incompressible flows. Comput. Phys. Rep. **10**, 77–146 (1989)
10. Davis, P.J.: The Schwarz Function and its Applications. Carus Mathematical Monographs No. 17, The Mathematical Association of America, Buffalo (1974)
11. Riccardi, G., Durante, D.: Velocity induced by a plane uniform vortex having the Schwarz function of its boundary with two simple poles. J. Appl. Math. Hindawi Pub. (2008). doi:10.1155/2008/586567
12. Wu, H.M., Overman, E.A., Zabusky, N.J.: Steady-state solutions of the Euler equations in two dimensions: rotating and translating V-states with limiting cases. I. Numerical algorithms and results. J. Comput. Phys. **53-1**, 42–71 (1984)

13. Overman, E.A.: Steady state solutions of the Euler-equations in two dimensions II. Local analysis of limiting V-states. SIAM J. Appl. Math. **46-5**, 765–800 (1986)
14. Crowdy, D.G.: The construction of exact multipolar equilibria of the two-dimensional Euler equations. Phys. Fluids **14-1**, 257–267 (2001)
15. Crowdy, D.G.: Exact solutions for rotating vortex arrays with finite-area cores. J. Fluid Mech. **469**, 209–235 (2002)
16. Constantin, P., Titi, E.S.: On the evolution of nearly circular vortex patches. Commun. Math. Phys. **119-2**, 177–198 (1988)
17. Legras, B., Zeitlin, V.: Conformal dynamics for vortex motions. Phys. Lett. A **167-3**, 265–271 (1992)
18. Riccardi, G.: Intrinsic dynamics of the boundary of a two-dimensional uniform vortex. J. Eng. Math. **50-1**, 51–74 (2004)
19. Davis, H.T.: Introduction to Nonlinear Differential and Integral Equations. Dover, New York (1962)
20. Tricomi, F.G.: Integral Equations. Dover, New York (1985)
21. Legras, B., Dritschel, D.G., Caillol, P.: The erosion of a distributed two-dimensional vortex in a background straining flow. J. Fluid Mech. **441**, 369–398 (2001)
22. Muskhelishvili, N.I.: Singular Integral Equations. Dover, New York (2008)
23. Riccardi, G.: Toward analytical contour dynamics. In: De Bernardis, E., Spigler, R., Valente, V. (eds.): Applied and industrial mathematics in Italy III (Advances in Mathematics for Applied Sciencies, vol. 82) pp. 496–507. World Scientific, Singapore (2009)
24. Cohn, H.: Conformal Mapping on Riemann Surfaces. McGraw-Hill, New York (1967)
25. Prosperetti, A.: Advanced Mathematics for Applications. Cambridge University Press, Cambridge (2011)